1   Revision 2

2

3   # Metasomatism-controlled hydrogen distribution in

4   # the Spitsbergen upper mantle

5

6   Wenting Tang[1], Hejiu Hui[1,2,*], Dmitri A. Ionov[3,4], Wei Chen[5], Lisha Zhang[1], Yongjiang

7   Xu[1]

8

9   **1.**   State Key Laboratory for Mineral Deposits Research & Lunar and Planetary

10   Science Institute, School of Earth Sciences and Engineering, Nanjing University,

11   Nanjing 210023, China

12   **2.**   CAS Center for Excellence in Comparative Planetology, Hefei 230026, China

13   **3.**   Géosciences Montpellier, Université de Montpellier, 34095 Montpellier, France

14   **4.**   State Key Laboratory of Isotope Geochemistry, Guangzhou Institute of

15   Geochemistry, Chinese Academy of Sciences, 510640 Guangzhou, China

16   **5.**   State Key Laboratory of Geological Processes and Mineral Resources, China

17   University of Geosciences, Wuhan 430074, China

18

19   * corresponding author: Hejiu Hui (hhui@nju.edu.cn)

1

Abstract

20

21   Hydrogen concentrations in minerals of peridotite xenoliths in alkali basaltic rocks

22   from Quaternary volcanoes in northwest Spitsbergen were measured using polarized

23   Fourier transform infrared spectroscopy (FTIR) to trace the effects of geologic processes

24   on hydrogen distribution in the continental lithospheric mantle. The mineral grains show

25   hydrogen profiles with lower concentrations at rims suggesting diffusive hydrogen loss

26   during the entrapment and transport of the xenoliths in magma. However, hydrogen

27   concentrations in the centers of the grains are uniform and appear to represent hydrogen

28   abundances in the Spitsbergen upper mantle. The olivine, orthopyroxene, and

29   clinopyroxene contain 1–10 ppm, 130–290 ppm, and 350–560 ppm H_2O, respectively.

30   Hydrogen abundances away from metasomatic melt conduits recorded by Type-1 xenoliths

31   are correlated with the concentrations of incompatible trace elements, indicating that

32   hydrogen distribution is related to mantle metasomatism, whereas hydrogen near the melt

33   conduits, recorded by Type-2 xenoliths, shows no regular correlations with incompatible

34   trace elements (except Nb in clinopyroxene) and may be affected by fractional

35   crystallization of amphibole in the conduits. Hydrogen contents decrease away from the

36   melt conduits, and are controlled by interaction between the depleted host mantle and

37   percolating metasomatic melts. Therefore, the metasomatic melt could have variably

38   hydrated the Spitsbergen upper mantle via different processes. The H_2O/Ce ratios of the

2

39   melt in equilibrium with clinopyroxene near the metasomatic melt conduits range from 93

40   to 218, i.e. fall within the oceanic island basalt (OIB) range. This is consistent with that the

41   metasomatic melt could have been derived from OIB-type sources evidenced by the Sr-Nd

42   isotope compositions of the xenoliths.

43

44   **Keywords**: Spitsbergen; lithospheric mantle; nominally anhydrous minerals;

45   hydrogen content; metasomatism

46

47   **Introduction**

48   Ultramafic xenoliths in volcanic rocks can directly sample the continental lithospheric

49   mantle (CLM). By far the most common mantle xenoliths in alkali basalts are spinel

50   peridotites that consist mainly of olivine, orthopyroxene, clinopyroxene and accessory

51   spinel, which are considered nominally anhydrous minerals (NAMs). However, trace

52   amounts of hydrogen can be incorporated in the crystal lattice defects of the silicate NAMs

53   to form hydroxyl by bonding to structural oxygen, and commonly called "water" in the

54   literature. Although present in only small amounts (a few to hundreds of ppm by weight of

55   H_2O), hydrogen may significantly influence physical and chemical properties of the CLM

56   (e.g., Mackwell et al. 1985; Bell and Rossman 1992; Hirth and Kohlstedt 1996; Hier-

57   Majumder et al. 2005; Wang et al. 2006; Yoshino et al. 2006) and therefore, affect mantle

3

58   processes. Conversely, partial melting and metasomatism in the mantle may affect

59   hydrogen distribution. Variations in hydrogen content have been attributed to partial

60   melting in the CLM of the South China Block (Hao et al. 2014; Zhang et al. 2018) and

61   Kilbourne Hole in the SW USA (Schaffer et al. 2019), but alternatively to metasomatism

62   in the CLM of the Kaapvaal craton (Peslier et al. 2012), the Siberian craton (Doucet et al.

63   2014), the Ontong Java plateau (Demouchy et al. 2015), and in the western Pacific mantle

64   wedge (Soustelle et al. 2010; Satsukawa et al. 2017).

65   Partial melting decreases hydrogen concentration in melting residues because it is

66   highly incompatible in NAMs. By contrast, metasomatism may add hydrogen to initially

67   "dry" residual mantle. The effects of partial melting and metasomatism can be disentangled

68   using the distribution of incompatible trace elements, especially rare earth elements (REE).

69   Both carbonatite and silicate metasomatism typically lead to enrichment of light REE

70   (LREE) in pyroxenes (e.g., Pearson et al. 2003), whereas residual mantle is depleted in

71   LREE relative to heavy and middle REE (HREE-MREE) (e.g., Walter 2003). The

72   compatibility of hydrogen is believed to be similar to that of LREE, such as La and Ce (e.g.,

73   Michael 1995; Danyushevsky et al. 2000; Dixon et al. 2002). However, the correlations

74   between hydrogen and LREE concentrations have only rarely been observed in mantle

75   peridotites (e.g., Peslier et al. 2017). Alternatively, it has been suggested that the

76   compatibility of hydrogen may be similar to that of MREE (Demouchy et al. 2015; Denis

4

77   et al. 2015). Furthermore, a positive correlation was observed in Ichinomegata peridotites

78   between hydrogen and Th/Ce (or U/Ce) in orthopyroxene, whereas a negative correlation

79   was found in clinopyroxene (Satsukawa et al. 2017). Positive correlations were observed

80   between pyroxene hydrogen content and bulk-rock La/Yb (and Ba/Nb) in Alligator Lake

81   lherzolites but not in Alligator Lake harzburgite (Kilgore et al. 2018). Finally, in the

82   mantle, hydrogen distribution between minerals can also be affected by sub-solidus

83   equilibration (Schaffer et al. 2019). Therefore, in xenoliths from the same volcano, and

84   even in the same mantle xenolith, hydrogen distribution in different minerals may be

85   complex, perhaps because of superposition of multiple mantle processes.

86   The lithospheric mantle underneath Spitsbergen has been shown to be affected by

87   metasomatism, resulting in LREE enrichments (e.g., Ionov 1998; Ionov et al. 2002a; Choi

88   et al. 2010; Griffin et al. 2012). A chromatographic model has been proposed to interpret

89   trace-element distribution patterns in Spitsbergen mantle xenoliths, which posits that the

90   enrichments in REE and other incompatible lithophile trace elements are linked to the

91   distance of a sample from metasomatic fluid conduits (Ionov et al. 2002a). Thus, the

92   Spitsbergen mantle xenoliths provide an opportunity to examine how hydrogen distribution

93   is correlated with metasomatism. In this study, hydrogen concentrations in olivine,

94   orthopyroxene, and clinopyroxene from typical Spitsbergen mantle xenoliths were

95   measured using Fourier transform infrared spectroscopy (FTIR). We further combined

5

96   major and trace-element compositions and isotope data for the xenoliths (Ionov et al. 1993,

97   1996, 2002a, 2002b; Ionov 1998) to explore processes controlling the distribution of

98   hydrogen in the Spitsbergen CLM.

99

100   **Geologic Setting and Samples**

101   Spitsbergen is the largest island of the Svalbard archipelago located between the North

102   Atlantic and the Arctic Oceans at similar distances from continental Norway, Greenland

103   and the North Pole. The Svalbard archipelago is the northwestern edge of the Eurasian

104   continent. It was part of the Laurentian continental margin and was connected to Greenland

105   until the opening of the North Atlantic Ocean and the formation of a transform fault zone

106   (Crane et al. 1982; Amundsen et al. 1987; Lawver et al. 1990; Faleide et al. 1993; Blythe

107   and Kleinspehn 1998). The Spitsbergen CLM was suggested to have been thinned by

108   delamination or mechanical erosion (Vågnes and Amundsen 1993; Griffin et al. 2012).

109   The mantle xenoliths were collected from hawaiitic to nepheline-basanitic rocks at

110   three Quaternary volcanoes (Sverre, Sigurd, and Halvdan) along the Breibogen Fault Zone

111   in the Bockfjord area, northwest Spitsbergen (Ionov et al. 2002a). The Quaternary

112   volcanism in this region may have been related to the activity of the spreading center and

113   transform fault zone ~150 km to the west (Amundsen et al. 1987; Sushchevskaya et al.

114   2008). The petrology, pressure–temperature (P-T) equilibration conditions, major and trace

6

115   element chemistry, and Sr-Nd-Pb isotopic compositions of Spitsbergen xenoliths that

116   experienced both modal and cryptic metasomatism have been studied in detail (Ionov et al.

117   1993, 1996, 2002b, 2002a; Ionov 1998).

118   A subset of thirteen xenoliths described in Ionov et al. (2002a) was analyzed for

119   hydrogen contents in this study (Table 1). The xenoliths can be divided into two main types

120   based on MREE-REE patterns (Ionov et al. 2002a). Type-2 rocks and their clinopyroxenes

121   show continuous enrichments in MREE and LREE; they represent the mantle within or

122   close to the metasomatic melt conduits, which experienced large-scale melt–rock

123   interaction and recorded geochemical fingerprints of the metasomatic agent (Ionov et al.

124   2002a). By contrast, Type-1 samples show flat HREE-MREE patterns, or MREE

125   depletions relative to the HREE, with steep "inflections" for all or only the most

126   incompatible LREE, and high La/Ce ratios. Two samples 26a and 4a-90-1 cannot be

127   grouped into these two types and thus are designated as "other" (Table 1). The

128   clinopyroxene REE pattern of xenolith 26a is relatively flat and the abundances are low,

129   whereas the clinopyroxene in vein sample 4a-90-1 has an REE pattern similar to Type-2

130   samples but with higher abundances of high field strength element (HFSE) and lower

131   HREE abundances (Ionov et al. 2002a). The Type-1 rocks formed away from the melt

132   conduits; they record compositional changes of the percolating melt due to

133   chromatographic effects of its interaction with host mantle, which was initially LREE-

134   depleted by melting (Ionov et al. 2002a). Thus, the distinctly different REE patterns in the

135   xenoliths were produced by a single metasomatic event at different distances from melt

136   conduits and different stages of melt fractionation (Ionov et al. 2002a). Type-1 xenolith 39-

137   86-1 is chemically heterogeneous (Ionov et al. 2002a), and its bulk and isotope

138   compositions may not be representative of specific degrees or stages of metasomatic melt

139   fractionation.

140

141   **Analytical Methods**

142   **Sample preparation**

143   The thirteen xenoliths studied here are spinel lherzolites or harzburgites, except for

144   wehrlite 4a-90-1, and show little or no post-eruption alteration. Some of them contain

145   volatile-bearing minerals (amphibole, apatite, or phlogopite) of mantle origin in addition

146   to NAMs (Table 1). Representative grains of olivine, orthopyroxene, and clinopyroxene

147   were hand-picked under a binocular microscope. Grains without visible inclusions, cracks

148   and alteration signs were cleaned with ethanol and deionized water in an ultrasonic cleaner,

149   dried under ambient conditions overnight and embedded in epoxy resin. Mineral grains

150   were doubly polished using a Buehler automatic polisher with polycrystalline diamond

151   suspension (9 μm, 3 μm, and 1 μm). The doubly-polished sections were cleaned with

152   acetone, ethanol, and deionized water. The thickness of the polished grains, measured using

153   a Mitutoyo Digimatic micrometer, ranged from 74 μm to 584 μm. The crystallographic

154   orientation of each polished mineral grain was determined by observing interference

155   figures under a petrographic microscope. Only optically clean grains with Bxo, Bxa, or

156   optic-normal interference figures were used for FTIR analyses. Before the analyses, the

157   polished sections were placed in a desiccator for ≥ 24 hours to eliminate potential surface

158   water contamination.

159

160   **Hydrogen analyses**

161   Polarized infrared spectra of olivine, orthopyroxene, and clinopyroxene were collected

162   using a Continuμm infrared microscope attached to a Nicolet iS50 FTIR spectrometer at

163   Nanjing University. The infrared spectra ranging from 650 cm^{-1} to 7000 cm^{-1} and with a

164   resolution of 4 cm^{-1} were obtained for a grain only when one of its principal axes of the

165   optical indicatrix (α, β, or γ) was parallel to the electric vector **E** of the incident light (Bell

166   et al. 1995; Libowitzky and Rossman 1996; Bell et al. 2003). At least three oriented grains

167   of each mineral in one sample were measured using polarized infrared light with a KBr

168   beam splitter and a liquid nitrogen-cooled mercury-cadmium-telluride (MCT-A) detector.

169   Each analysis consisted of 256 scans in a pre-dried air environment to minimize

170   interference from atmospheric water vapor. Depending on the grain size and the

171   distribution of fractures and inclusions in the grain, the aperture size varied from 50 μm ×

9

172   50 μm to 80 μm × 80 μm. At least three spots in different areas of each grain were analyzed

173   to determine whether hydrogen was uniformly distributed.

174   The baseline of each spectrum normalized to 1 cm thickness was manually corrected

175   with the Omnic software. The O-H absorbance was determined by integrating the area

176   under the O-H vibration bands. The modified Beer–Lambert equation was used to convert

177   the sum of the integrated absorbance for $\mathbf{E}$//α, //β, //γ ($A_{tot} = A_\alpha + A_\beta + A_\gamma$, normalized to 1

178   cm) to the hydrogen concentration C_H (ppm by weight of H_2O) in olivine, orthopyroxene,

179   and clinopyroxene:

180                                    $$C_H = A_{tot}/I$$

181   where I is the integral specific absorption coefficient (Table 2). Uncertainties generated in

182   each step are grain thickness (<2 %), grain orientation (<5 %), baseline correction (<10 %),

183   and the reported absorption coefficient (Table 2). The overall uncertainty of the determined

184   hydrogen concentration is typically ≤20 %.

185

186   **Trace element analyses**

187   *In situ* trace element analyses of clinopyroxene in four xenoliths were performed using

188   a Thermo Scientific iCAP-Qc ICP-MS coupled to a RESOlution 193-nm laser ablation

189   system at the State Key Laboratory of Geological Processes and Mineral Resources

190   (GPMR), China University of Geosciences (Wuhan). NIST SRM 612 glass standard was

10

191   used to correct instrument drift. USGS reference glasses BIR-1G, BCR-2G, and BHVO-

192   2G were used as external standards for calibration. NIST and USGS glass standards were

193   repeatedly analyzed after every five to eleven unknowns. Standards and clinopyroxenes

194   were analyzed using a laser beam with a spot size of 33 μm, repetition rate of 10 Hz, and

195   energy density of ~5 J/cm^2. Each analysis consisted of 30 s of background acquisition and

196   40 s of data acquisition. Data reduction was performed using ICPMSDataCal software (Liu

197   et al. 2008). Analytical uncertainties for most trace elements were within 10 % and better

198   than 5 % for REEs.

199

200   **Results**

201   **FTIR spectra**

202   Olivine in the Spitsbergen xenoliths has two groups of O-H absorption bands, at 3700–

203   3450 cm^{-1} (Group I) and 3450–3100 cm^{-1} (Group II) (Fig. 1a and 1b), which have also been

204   observed in olivine from other localities (e.g., Miller et al. 1987; Bell et al. 2003;

205   Mosenfelder et al. 2006; Li et al. 2008; Baptiste et al. 2015; Peslier et al. 2015). No O-H

206   bands typically associated with serpentine or talc (Miller et al. 1987; Mosenfelder et al.

207   2006) were observed in the Spitsbergen olivine. The O-H bands in the spectra obtained

208   with $\mathbf{E}//\gamma$ have the strongest absorbance relative to those with $\mathbf{E}//\alpha$ and $\mathbf{E}//\beta$ in Group I,

209   whereas in Group II, the O-H absorbance with $\mathbf{E}//\beta$ is the strongest (Fig. 1a and 1b). All

210   the olivines have O-H bands at 3572, 3525, and 3225 cm^{-1}. The O-H band at 3600 cm^{-1}

211   with **E**//γ are strong only in wehrlite 4a-90-1 (Fig. 1b), and much weaker in samples 318,

212   318-1 and 43-86. Very small bands were observed at 3355, 3325, and 3306 cm^{-1} in the

213   spectra obtained with **E**//β of samples 318, 26a, 28b, and 4-36-90 (Fig. 1a). No Group I O-

214   H bands were observed in the spectra obtained with **E**//α of nine samples in this study (Fig.

215   1b).

216   The O-H absorption bands (3700–2800 cm^{-1}) of Spitsbergen orthopyroxene (Fig. 1c)

217   resemble those previously reported for mantle orthopyroxene (e.g., Skogby et al. 1990;

218   Bell et al. 1995; Peslier et al. 2002; Li et al. 2008; Sundvall and Stalder 2011; Mosenfelder

219   and Rossman 2013a; Hui et al. 2015). The strongest O-H absorbance occurs in the polarized

220   spectra obtained with **E**//γ. Prominent O-H absorption bands occur at 3570 cm^{-1} (not

221   always present) and 3520 cm^{-1} on spectra obtained with **E**//γ, at 3600 cm^{-1} and 3420 cm^{-1}

222   on spectra obtained with **E**//β, and at 3600 cm^{-1} on spectra obtained with **E**//α. Smaller

223   bands are often present at low wavenumbers (3400–3000 cm^{-1}; Fig. 1c).

224   The O-H vibration bands of Spitsbergen clinopyroxene occur at 3700–3000 cm^{-1} (Fig.

225   1d), similar to those of clinopyroxene from other locations (e.g., Skogby et al. 1990; Peslier

226   et al. 2002; Li et al. 2008; Sundvall and Stalder 2011; Mosenfelder and Rossman 2013b).

227   Spectra obtained with **E**//α or **E**//β have characteristic O-H bands at 3640 cm^{-1}. The spectra

12

228   obtained with $\mathbf{E}//\gamma$ show two dominant O-H bands at 3525 cm^{-1} and 3460 cm^{-1}. Absorbance

229   with $\mathbf{E}//\gamma$ is slightly weaker than that with $\mathbf{E}//\alpha$ or $\mathbf{E}//\beta$.

230

231   **Hydrogen concentrations**

232   Hydrogen is heterogeneously distributed in the olivine grains, as indicated by the

233   profiles of Group I O-H absorbance (Figs. 2a–b and 3a). The Group II O-H absorbances in

234   most of the olivine grains are rather uniform, although some grains from samples 318, 318-

235   1, 28b, and 4-36-90 have slightly weaker Group II O-H absorbances at their rims than in

236   their cores (Fig. 2c). Despite the heterogeneous hydrogen distribution at grain rims, all

237   olivine grains show uniform hydrogen distribution in the cores, as indicated by the O-H

238   absorbance plateaus (Figs. 2 and 3a). The hydrogen concentrations in the olivine

239   determined using the polarized O-H absorbances in the plateau areas at grain centers range

240   from 1 to 10 ppm (Table 2).

241   Uneven distribution of hydrogen with plateau-shaped concentration profile was also

242   observed in orthopyroxene grains of samples 318-1, 4-25-90 and 26a (Fig. 3b). Uniform

243   hydrogen distribution was observed in all orthopyroxene cores, where the hydrogen

244   contents range from 130 to 290 ppm (Table 2).

245   In clinopyroxene grains, the core-rim difference of O-H absorbance only occurs in

246   samples 43-86 and 318-1 (Fig. 3c), and the hydrogen distribution in the cores is uniform.

13

247   Hydrogen concentrations were not determined in clinopyroxene grains with exsolution

248   lamellae in sample 39-86-1 (Ionov et al. 2002a). Calculated hydrogen concentrations in the

249   clinopyroxene range from 350 to 560 ppm (Table 2).

250

251   **Trace-element compositions in clinopyroxene**

252   Trace element compositions were measured in clinopyroxene from samples 28b, 39-

253   86-1, 43-86, and 318-1 (Table 3). Multi-spot analyses of clinopyroxene grains revealed

254   uniform trace element distribution. Our data for clinopyroxene of sample 318-1 (Table 3)

255   are consistent with previous measurements of clinopyroxene in this sample (Ionov et al.

256   2002a; Fig. 4a–b). In terms of REE distribution patterns, samples 28b and 39-86-1 belong

257   to the Type-1 group, and sample 43-86 is a Type-2 xenolith (Fig. 4c–d).

258

259   **Discussion**

260   **Hydrogen loss from xenoliths and preservation of mantle hydrogen concentrations**

261   Hydrogen is unevenly distributed in olivine grains as well as in some pyroxene grains

262   of the Spitsbergen xenoliths (Figs. 2–3), but the distribution of major and trace elements in

263   the minerals is uniform (Ionov et al. 2002a). Therefore, the plateau-shaped O-H absorbance

264   profiles in the mineral grains stem from hydrogen diffusive degassing likely during

265   xenolith ascent to the surface. Such hydrogen loss is common in mantle xenoliths (e.g.,

14

266   Demouchy et al. 2006; Peslier and Luhr 2006; Li et al. 2008; Denis et al. 2013; Doucet et

267   al. 2014; Peslier et al. 2015).

268   One-dimensional (1-D) diffusion modeling (Shewmon 1989) was carried out to fit

269   the O-H absorbance profiles in the mineral grains (Figs. 2–3). The hydrogen diffusivities

270   (Table 4) were calculated using the equations in Xu et al. (2019). The calculated

271   diffusivities in olivine are within the range of literature data (e.g., Xu et al. 2019) and the

272   diffusivities in pyroxene are similar to those literature values (e.g., Ingrin et al. 1995;

273   Stalder and Skogby 2003), within an order of magnitude difference. The diffusion profiles

274   for coexisting olivine and pyroxenes were fit assuming that hydrogen diffusion in

275   coexisting minerals occurred at the same time (i.e., for the same length of time) and thus

276   the diffusion temperature and duration could be calculated simultaneously (Fig. 3; Xu et al.

277   2019). The inferred diffusion temperatures (750–830 °C; Fig. 3) are lower than xenolith

278   equilibrium temperatures in the mantle (890–1025 °C; Table 1) suggesting that the

279   hydrogen diffusive degassing could have taken place mainly at shallow depths or at the

280   surface when the xenoliths were entrained in cooling lava. For the samples in which

281   hydrogen loss was observed only in olivine and not in coexisting pyroxene (Fig. 2), the

282   diffusion and equilibrium temperatures were assumed to be equal, such that diffusion

283   duration could be calculated (Peslier et al. 2015). Overall, the results from diffusion

284   modeling of Group I O-H absorbance show that the diffusion time ranges from 0.4 to 30

15

285   hours (Figs. 2–3), which appears to be a realistic duration for xenolith transport and cooling

286   in pyroclastic deposits at the surface.

287   To summarize, the hydrogen diffusion profiles (Figs. 2–3) indicate that some hydrogen

288   was lost from the minerals during xenolith transport and/or emplacement. Water fugacity

289   in the host magma decreases on ascent owing to decompression, which leads to degassing

290   of xenoliths entrained in the magma to form the plateau-shaped hydrogen profiles in mantle

291   minerals. Importantly, our FTIR hydrogen diffusion profiles show plateaus at grain centers

292   for all the mineral grains, which we interpret as recording hydrogen concentrations before

293   degassing. Furthermore, hydrogen concentrations in the grain centers of olivine and

294   coexisting pyroxenes appears to be equilibrated (see next subsection; Fig. 5). Therefore,

295   we conclude that the hydrogen abundances measured in the grain-core plateaus (Table 2)

296   represent those of the minerals in the Spitsbergen CLM.

297

298   **Inter-mineral hydrogen equilibrium**

299   The hydrogen concentrations in olivine and coexisting pyroxenes in the Spitsbergen

300   xenoliths show positive linear covariations (Fig. 5) suggesting equilibrium hydrogen

301   distribution between these minerals. To further evaluate whether hydrogen was in

302   equilibrium between these phases before the diffusive degassing, the pyroxene/olivine

303   concentration ratios can be compared to experimentally determined inter-mineral hydrogen

16

304   partition coefficients. Because published experimental data vary widely (Fig. 5), a range of

305   experimental partition coefficients for different mantle conditions (Hauri et al. 2006;

306   Tenner et al. 2009; Novella et al. 2014; Demouchy et al. 2017) is compared here with our

307   data to evaluate inter-mineral hydrogen equilibrium in Spitsbergen xenoliths (Fig. 5).

308   The pyroxene/olivine concentration ratios in the Spitsbergen xenoliths ($K_H^{Opx/Ol} =$

309    $C_H^{Opx}/C_H^{Ol} = 29$–116 and $K_H^{Cpx/Ol} = C_H^{Cpx}/C_H^{Ol} = 56$–$135$) are systematically higher than

310   experimental partition coefficients (Fig. 5a and b). The clinopyroxene to orthopyroxene

311   hydrogen concentration ratios ($K_H^{Cpx/Opx} = C_H^{Cpx}/C_H^{Opx}$) range from 1.8 to 2.6, which is

312   close to experimental data (Novella et al. 2014; Fig. 5c) and similar to values found for

313   peridotites worldwide (e.g., Peslier et al. 2002, 2012; Doucet et al. 2014; Hui et al. 2015;

314   Peslier and Bizimis 2015).

315   The discrepancy between the pyroxene/olivine hydrogen concentration ratios in the

316   Spitsbergen xenoliths and experimental partition coefficients may stem from different *P-T*

317   conditions of peridotite equilibration in the mantle and in the laboratory experiments. The

318   laboratory experiments were performed at solidus conditions, which are higher than the

319   sub-solidus equilibration temperatures of Spitsbergen xenoliths (Table 1). Hydrogen in

320   Spitsbergen minerals, as well as major and other trace elements, could have equilibrated at

321   sub-solidus conditions, similar to the mantle minerals beneath the Rio Grande Rift

322   (Schaffer et al. 2019). The linear correlations between equilibrium temperature of the

17

323   xenoliths and hydrogen concentration in their minerals (Fig. 6) are consistent with this sub-

324   solidus equilibration, which could have resulted in hydrogen re-equilibration between

325   Spitsbergen olivine and coexisting pyroxene after the end of melt percolation and a

326   temperature decrease below the solidus. Hydrogen contents of Spitsbergen mantle minerals

327   at solidus temperature (assumed to be 1350 °C, the temperature of Spitsbergen

328   asthenosphere; Vågnes and Amundsen 1993) can be calculated following the method in

329   Schaffer et al. (2019) (Table 4). The calculated hydrogen concentration ratios are $K_H^{Opx/Ol}$

330   = 13–19, $K_H^{Cpx/Ol}$ = 14–21, and $K_H^{Cpx/Opx}$ = 1.1, close to the experimental values

331   determined by Hauri et al. (2006), probably because the pressure range in that experimental

332   study is also similar to that of Spitsbergen lithosphere (Fig. 5). Therefore, the discrepancy

333   between Spitsbergen hydrogen distributions and experimentally determined partition

334   coefficients could have been caused by sub-solidus equilibration in the mantle. In

335   conclusion, the hydrogen distribution between pyroxenes and olivine in the Spitsbergen

336   mantle xenoliths could be at equilibrium.

337

338   **Metasomatic control of hydrogen distribution in Spitsbergen mantle**

339   Partial melting and metasomatism may control hydrogen distribution in the mantle.

340   The Spitsbergen peridotites initially formed as residues of moderate to high degrees of melt

341   extraction from a fertile source (Ionov et al. 2002a). Hydrogen is incompatible during

18

342   mantle partial melting and its abundances in the NAMs decrease at higher melting degrees.

343   Commonly used melting indices for mantle residues (e.g., Boyd 1989; Niu et al. 1997) are

344   olivine Mg# [Mg/(Mg+Fe)$_{at}$] and spinel Cr# [Cr/(Cr+Al)$_{at}$], which increase with melting

345   degrees, and whole-rock Al$_2$O$_3$ and HREE in clinopyroxene, which decrease with melting.

346   However, no obvious correlations exist between the hydrogen abundances in NAMs and

347   the partial melting indices in the Spitsbergen xenoliths (Fig. 7). If such correlation existed,

348   they must have been overprinted by subsequent mantle events, i.e., metasomatism.

349   Previous studies have established that mantle metasomatism in the Spitsbergen mantle

350   is produced by melts that experience "chromatographic" fractionation as they percolate

351   through host peridotites (Ionov et al. 2002a). This process has several key aspects. First,

352   the initial metasomatic melt is enriched in a broad range of incompatible trace elements as

353   it leaves the melt conduit, and is abundant (high melt/rock ratios) close to the conduit. This

354   is why melt equilibrates with minerals in the host peridotites affected by melt-rock reaction

355   close to the melt conduit. However, as the melt percolates through residual peridotites

356   (depleted in incompatible elements by melt extraction), it becomes selectively depleted in

357   trace elements with higher mineral/melt distribution coefficients (e.g., MREE-HREE),

358   which preferentially partition to host peridotites (initially depleted in these elements), but

359   retains much of its initial load of more incompatible elements like hydrogen, La, Ce, Th.

360   Second, the melt/rock ratio decreases as the melt percolation proceeds because the melt is

19

361   consumed by reaction with the host. As a result, the metasomatism far from the melt

362   conduit and near the percolation front is implemented via additions (mixing) of small

363   amounts of the fractionated melt with the depleted host rather than equilibrium exchange

364   of the melt with the host.

365   Two types of metasomatized Spitsbergen xenoliths were previously identified based

366   on trace element patterns in bulk rocks and minerals (e.g., Ionov et al. 1993, 2002a; Ionov

367   1998). Type-1 rocks have "spoon-shaped" REE patterns with nearly flat or gently sloping

368   HREE to MREE distribution, often with a minimum between Pr and Sm, followed by a

369   continuous increase in the most incompatible LREE, Th and U with high La/Ce ratios (Fig.

370   4c; Ionov et al. 2002a). The Type-1 xenoliths were interpreted as interaction or mixing

371   products of residual, LREE-depleted mantle with small amounts of fractionated melt that

372   penetrated far from its initial conduit by intergranular percolation.

373   Hydrogen concentrations in NAMs in the Type-1 Spitsbergen xenoliths show positive

374   linear correlations with those of the most incompatible trace elements: notably La, Th and

375   La/Yb ratios in clinopyroxene (Fig. 8), and with whole-rock La, Nb and Th and Zr/Hf ratios

376   (Fig. 9). Hydrogen concentrations in NAMs also correlate with Nd isotope ratios in

377   clinopyroxene (Figs. 10a2, 10b2, and 10c2). All these suggest that the distribution of both

378   hydrogen and other highly incompatible trace elements was controlled by the same

20

379   metasomatic processes and media, i.e., percolation of water-bearing silicate melts from

380   conduits into melt-depleted host peridotites (Ionov et al. 2002a; Ionov 1998).

381   The REE patterns in Type-2 xenoliths (Fig. 4d) are attributed to equilibration with

382   metasomatic melts close to the melt conduits (Ionov et al. 2002a). In contrast to Type-1

383   xenoliths, no obvious correlations are seen in Type-2 xenoliths between hydrogen in NAMs

384   and trace-element or isotope compositions of clinopyroxenes, or whole-rock trace element

385   compositions (Figs. 8–10), apart from positive correlations of hydrogen in NAMs with Nb

386   in clinopyroxene (Figs. 11a1, 11b1, and 11c1). On the other hand, hydrogen in NAMs

387   shows linear correlations with whole-rock Nb abundances in Type-1 xenoliths (Figs. 11a2,

388   11b2, and 11c2). Niobium is more compatible in hydrous mineral amphibole (e.g., Chazot

389   et al. 1996; Ionov et al. 1997; Downes et al. 2004), which is common in Type-2 xenoliths,

390   than in NAMs, and the correlations between hydrogen in NAMs and Nb in clinopyroxene

391   may be due to fractionation of amphibole from initial metasomatic melt in or near the melt

392   conduit, which imparts a Nb-depletion signature on the melt that moves away from the

393   initial conduit (Ionov et al. 2002a). The narrow Nd and Sr isotope composition ranges in

394   Type-2 clinopyroxene (Ionov et al. 2002b) may also be linked to crystallization of hydrous

395   minerals.

396   Type-1 xenolith 315-6 contains amphibole. However, amphibole trace element

397   abundances in this sample are distinct from those in the Type-2 xenoliths likely because

21

398   this sample was located far from the metasomatic melt conduit (Ionov et al. 2002a). This

399   is consistent with the linear correlations between hydrogen in NAMs and incompatible

400   trace elements in clinopyroxene in Type-1 xenoliths, including sample 315-6 (Figs. 8–10).

401   In summary, metasomatism played a large role in controlling the hydrogen distribution

402   in the Spitsbergen CLM. The chromatographic effects of melt percolation (Ionov et al.

403   2002a) were major factors that controlled the distribution of incompatible trace elements,

404   including hydrogen, in the mantle far from the metasomatic melt conduits. Type-2

405   xenoliths represent the mantle near the metasomatic melt conduits, which may have

406   reached equilibrium with the metasomatic melt. Hydrogen incorporation in the NAMs of

407   Type-2 xenoliths may have been controlled by crystal fractionation of amphibole. As the

408   metasomatic melt infiltrated the Spitsbergen CLM, the melt became progressively depleted

409   in incompatible trace elements, including hydrogen, as they partitioned into host rocks.

410   Overall, this metasomatic event hydrated the Spitsbergen CLM, but the hydrogen additions

411   decreased with the distance from the metasomatic melt conduits.

412

413   **Sources of the metasomatic melt**

414   The H_2O/Ce ratio has been used to trace the source regions of metasomatic melt (e.g.,

415   Michael 1995; Plank et al. 2009; Peslier et al. 2012; Doucet et al. 2014; Hui et al. 2015).

416   The isotope data suggest that Type-2 xenoliths could be related to metasomatism by OIB-

22

417   type silicate melts (Ionov et al. 2002b). This relationship is also consistent with the

418   similarity of REE distribution patterns between Type-2 clinopyroxene and OIB (Sun and

419   McDonough 1989; Ionov et al. 2002a). The Type-2 Spitsbergen xenoliths that show

420   metasomatic imprints of melt percolation appear to represent the mantle that equilibrated

421   with the initial OIB-related metasomatic melt (Ionov et al. 2002a). Therefore, the H_2O/Ce

422   ratios of the melts in equilibrium with Type-2 clinopyroxenes may be used to infer those

423   of the initial melt (Fig. 12a). Applying $K_H^{Cpx/melt}$ and $K_{Ce}^{Cpx/melt}$ (Table 4), yields H_2O/Ce

424   ratios of the melts in equilibrium with the Type-2 clinopyroxenes ranging from 93 to 218.

425   This range overlaps with that for mid-ocean ridge basalts (MORB: 155 to 280; Michael

426   1995). The melt H_2O/Ce ratios are within the range for ocean island basalts (OIB: ~50 to

427   350; Dixon and Clague 2001; Dixon et al. 2002; Wallace 2002; Workman et al. 2006;

428   Cabral et al. 2014; Kendrick et al. 2014, 2015; Bizimis and Peslier 2015). In contrast, the

429   H_2O/Ce ratios are lower than those of arc lavas, which range from 200 to 20000 (Fig. 12a;

430   Plank et al. 2009). The geochemical constraints on the metasomatic melts suggest that

431   Spitsbergen mantle may have been affected by the upwellings related to Iceland plume,

432   consistent with geophysical constrains (Vågnes and Amundsen 1993).

433   The metasomatism in the Spitsbergen mantle could be modeled as a mixing process of

434   depleted CLM with an OIB-type metasomatic melt because the H_2O/Ce (or H_2O/La) ratios

435   of the hypothetical melts equilibrated with the Spitsbergen clinopyroxenes are correlated

23

436   with Sr-Nd isotope compositions of the clinopyroxenes (Fig. 12b–d). In the mixing model,

437   Type-2 xenoliths were defined as the enriched end-member, which was in equilibrium with

438   the metasomatic melt, and the least-metasomatized Type-1 xenolith (39-86-2) represents

439   the depleted end-member (i.e., the mantle before the metasomatism). The mixing model

440   for H_2O/Ce–Sr isotope (Fig. 12b) suggests that 40–80 % of these elements in Type-1

441   xenoliths originate from the enriched end-member whereas the H_2O/Ce (or H_2O/La)–Nd

442   isotope mixing model yields a lower range of 10–50 % (Figs. 12c and 12d). The

443   discrepancy in the two mixing models may stem from Sr-Nd elemental and isotope

444   decoupling due to chromatographic effects during metasomatism (Ionov et al. 2002b).

445

446   **Viscosity of Spitsbergen upper mantle**

447   The thickness of Spitsbergen lithosphere inferred from the geotherm is ~50 km, much

448   thinner than a normal lithosphere of 125 km (Vågnes and Amundsen 1993). Hydrogen can

449   decrease the viscosity of olivine and thus that of lithospheric mantle (e.g., Mackwell et al.

450   1985; Hirth and Kohlstedt 1996; Mei and Kohlstedt 2000a, 2000b). Therefore, it is

451   necessary to check whether the thinning of Spitsbergen lithosphere could be related to the

452   mantle hydrogen content. The effective viscosities calculated using olivine hydrogen

453   content and equilibrium temperature at 1.5 GPa range from 5.1×10^{22} to 5.2×10^{25} Pa·s (Fig

454   13; Table 4), much higher than the range for global asthenosphere (2.7×10^{17}–2×10^{19} Pa·s;

24

455   Craig and McKenzie 1986; Hager 1991; Pollitz et al. 1998; Larson et al. 2005). Therefore,

456   the effect of hydrogen on the thinning of Spitsbergen lithosphere may be negligible. On the

457   other hand, a high heat flow of ~130 mW·m^{-2} has been inferred in the Bockfjord area

458   (Vågnes and Amundsen 1993), where Spitsbergen xenoliths were collected. The viscosity

459   of Spitsbergen olivine at 1350 °C (Spitsbergen asthenosphere temperature; Vågnes and

460   Amundsen 1993) ranges from 1.7×10^{18} to 5.5×10^{18} Pa·s, i.e. within the viscosity range of

461   global asthenosphere. Therefore, high temperature may be the main factor to cause the

462   mechanical erosion of Spitsbergen lithosphere (Amundsen et al. 1987; Vågnes and

463   Amundsen 1993; Khutorskoi et al. 2009), similar to observations on the Tanzanian craton

464   (Hui et al. 2015).

465

466   **Implications**

467   The compatibility of hydrogen has been suggested to be similar to that of LREE, such

468   as La and Ce (e.g., Michael 1995; Danyushevsky et al. 2000; Dixon et al. 2002). However,

469   correlations between hydrogen and LREE concentrations in mantle peridotites have rarely

470   been reported. In Spitsbergen xenoliths, positive correlations between hydrogen and

471   incompatible trace elements suggest that mantle metasomatism was the main factor

472   controlling hydrogen distribution in the Spitsbergen CLM. The percolating melt evolved

473   from moderately wet to dry as it moved away from the melt conduits and thus variably

25

474 hydrated the Spitsbergen upper mantle during the metasomatism. In this metasomatic event,

475 different processes could have generated different correlations hydrogen and incompatible

476 trace elements (Figs. 8–11).

477 The H_2O/Ce ratios calculated for melts equilibrated with clinopyroxenes in the Type-

478 2 xenoliths range from 93 to 218. Together with Sr-Nd isotope compositions of the

479 Spitsbergen xenoliths (Ionov et al. 2002b) and high heat flow of ~130 $mW·m^{-2}$ in

480 Spitsbergen (Vågnes and Amundsen 1993), this leads us to conclude that the metasomatic

481 melt may be plume-related. The viscosity contrast shows that hydrogen may not contribute

482 significantly to the thinning of Spitsbergen lithosphere, but high temperature has played an

483 important role in this mechanical erosion process.

484

26

References

493

494   Amundsen, H.E.F., Griffin, W.L., and O'Reilly, S.Y. (1987) The lower crust and upper

495   mantle beneath northwestern Spitsbergen: evidence from xenoliths and geophysics.

496   Tectonophysics, 139, 169–185.

497   Bai, Q., and Kohlstedt, D.L. (1993) Effects of chemical environment on the solubility and

498   incorporation mechanism for hydrogen in olivine. Physics and Chemistry of Minerals,

499   19, 460–471.

500   Baptiste, V., Tommasi, A., Vauchez, A., Demouchy, S., and Rudnick R.L. (2015)

501   Deformation, hydration, and anisotropy of the lithospheric mantle in an active rift:

502   Constraints from mantle xenoliths from the North Tanzanian Divergence of the East

503   African Rift. Tectonophysics, 639, 34–55.

504   Bédard, J.H. (2014) Parameterizations of calcic clinopyroxene-Melt trace element partition

505   coefficients. Geochemistry, Geophysics, Geosystems, 15, 303–336.

506   Bell, D.R., and Rossman, G.R. (1992) Water in Earth's mantle: the role of nominally

507   anhydrous minerals. Science, 255, 1391–1397.

508   Bell, D.R., Ihinger, P.D., and Rossman, G.R. (1995) Quantitative analysis of trace OH in

509   garnet and pyroxenes. American Mineralogist, 80, 465–474.

510   Bell, D.R., Rossman, G.R., Maldener, J., Endisch, D., and Rauch, F. (2003) Hydroxide in

511   olivine: A quantitative determination of the absolute amount and calibration of the IR

512   spectrum. Journal of Geophysical Research, 108, 2105.

513   Bizimis, M., and Peslier, A.H. (2015) Water in Hawaiian garnet pyroxenites: Implications

514   for water heterogeneity in the mantle. Chemical Geology, 397, 61–75.

515   Blythe, A.E., and Kleinspehn, K.L. (1998) Tectonically versus climatically driven

516   Cenozoic exhumation of the Eurasian plate margin, Svalbard: Fission track analyses.

517   Tectonics, 17, 621–639.

518   Boyd, F.R. (1989) Compositional distinction between oceanic and cratonic lithosphere.

519   Earth and Planetary Science Letters, 96, 15–26.

520   Brey, G.P., and Köhler, T. (1990) Geothermobarometry in four-phase lherzolites II. New

521   thermobarometers, and practical assessment of existing thermobarometers. Journal of

522   Petrology, 31, 1353–1378.

523   Cabral, R.A., Jackson, M.G., Koga, K.T., Rose-Koga, E.F., Hauri, E.H., Whitehouse, M.J.,

524   Price, A.A., Day, J.M.D., Shimizu, N., and Kelley, K.A. (2014) Volatile cycling of

525   H_2O, CO_2, F, and Cl in the HIMU mantle: A new window provided by melt inclusions

526   from oceanic hot spot lavas at Mangaia, Cook Islands. Geochemistry, Geophysics,

527   Geosystems, 15, 4445–4467.

528 Chazot, G., Menzies, M.A., and Harte, B. (1996) Determination of partition coefficients

529   between apatite, clinopyroxene, amphibole, and melt in natural spinel lherzolites from

530   Yemen: Implications for wet melting of the lithospheric mantle. Geochimica et

531   Cosmochimica Acta, 60, 423–437.

532 Choi, S.H., Suzuki, K., Mukasa, S.B., Lee, J.-I., and Jung, H. (2010) Lu-Hf and Re-Os

533   systematics of peridotite xenoliths from Spitsbergen, western Svalbard: Implications

534   for mantle-crust coupling. Earth and Planetary Science Letters, 297, 121–132.

535 Craig, C.H., and McKenzie, D. (1986) The existence of a thin low-viscosity layer beneath

536   the lithosphere. Earth and Planetary Science Letters, 78, 420–426.

537 Crane, K., Eldholm, O., Myhre, A.M., and Sundvor, E. (1982) Thermal implications for

538   the evolution of the Spitsbergen Transform Fault. Tectonophysics, 89, 1–32.

539 Danyushevsky, L.V., Eggins, S.M., Falloon, T.J., and Christie, D.M. (2000) H_2O

540   abundance in depleted to moderately enriched mid-ocean ridge magmas; part I:

541   incompatible behaviour, implications for mantle storage, and origin of regional

542   variations. Journal of Petrology, 41, 1329–1364.

543 Demouchy, S., Jacobsen, S.D., Gaillard, F., and Stern, C.R. (2006) Rapid magma ascent

544   recorded by water diffusion profiles in mantle olivine. Geology, 34, 429–432.

29

545   Demouchy, S., Ishikawa, A., Tommasi, A., Alard, O., and Keshav, S. (2015)

546   Characterization of hydration in the mantle lithosphere: Peridotite xenoliths from the

547   Ontong Java Plateau as an example. Lithos, 212–215, 189–201.

548   Demouchy, S., Shcheka, S., Denis, C.M.M., and Thoraval, C. (2017) Subsolidus hydrogen

549   partitioning between nominally anhydrous minerals in garnet-bearing peridotite.

550   American Mineralogist, 102, 1822–1831.

551   Denis, C.M.M., Demouchy, S., and Shaw, C.S.J. (2013) Evidence of dehydration in

552   peridotites from Eifel Volcanic Field and estimates of the rate of magma ascent.

553   Journal of Volcanology and Geothermal Research, 258, 85–99.

554   Denis, C.M.M., Alard, O., and Demouchy, S. (2015) Water content and hydrogen

555   behaviour during metasomatism in the uppermost mantle beneath Ray Pic volcano

556   (Massif Central, France). Lithos, 236–237, 256–274.

557   Dixon, J.E., and Clague, D.A. (2001) Volatiles in basaltic glasses from Loihi Seamount,

558   Hawaii: evidence for a relatively dry plume component. Journal of Petrology, 42, 627–

559   654.

560   Dixon, J.E., Leist, L., Langmuir, C., and Schilling, J.-G. (2002) Recycled dehydrated

561   lithosphere observed in plume-influenced mid-ocean-ridge basalt. Nature, 420, 385–

562   389.

563   Doucet, L.S., Peslier, A.H., Ionov, D.A., Brandon, A.D., Golovin, A.V., Goncharov, A.G.,

564   and Ashchepkov, I.V. (2014) High water contents in the Siberian cratonic mantle

565   linked to metasomatism: An FTIR study of Udachnaya peridotite xenoliths.

566   Geochimica et Cosmochimica Acta, 137, 159–187.

567   Downes, H., Beard, A., and Hinton, R. (2004) Natural experimental charges: an ion-

568   microprobe study of trace element distribution coefficients in glass-rich hornblendite

569   and clinopyroxenite xenoliths. Lithos, 75, 1–17.

570   Faleide, J.I., Vågnes, E., and Gudlaugsson, S.T. (1993) Late Mesozoic-Cenozoic evolution

571   of the south-western Barents Sea in a regional rift-shear tectonic setting. Marine and

572   Petroleum Geology, 10, 186–214.

573   Griffin, W.L., Nikolic, N., O'Reilly, S.Y., and Pearson, N.J. (2012) Coupling, decoupling

574   and metasomatism: Evolution of crust–mantle relationships beneath NW Spitsbergen.

575   Lithos, 149, 115–135.

576   Hager, B.H. (1991) Mantle Viscosity: A Comparison of Models from Postglacial Rebound

577   and from the Geoid, Plate Driving Forces, and Advected Heat Flux. In R. Sabadini, K.

578   Lambeck, and E. Boschi, Eds., Glacial Isostasy, Sea-Level and Mantle Rheology pp.

579   493–513. Springer Netherlands, Dordrecht.

580   Hao, Y., Xia, Q., Li, Q., Chen, H., and Feng, M. (2014) Partial melting control of water

581   contents in the Cenozoic lithospheric mantle of the Cathaysia block of South China.

582   Chemical Geology, 380, 7–19.

583   Hauri, E.H., Gaetani, G.A., and Green, T.H. (2006) Partitioning of water during melting of

584   the Earth's upper mantle at H_2O-undersaturated conditions. Earth and Planetary

585   Science Letters, 248, 715–734.

586   Hier-Majumder, S., Anderson, I.M., and Kohlstedt, D.L. (2005) Influence of protons on

587   Fe-Mg interdiffusion in olivine. Journal of Geophysical Research, 110, B02202.

588   Hirth, G., and Kohlstedt, D. (1996) Water in the oceanic upper mantle: Implications for

589   rheology, melt extraction and the evolution of the lithosphere. Earth and Planetary

590   Science Letters, 144, 93-108.

591   Hui, H., Peslier, A.H., Rudnick, R.L., Simonetti, A., and Neal, C.R. (2015) Plume-cratonic

592   lithosphere interaction recorded by water and other trace elements in peridotite

593   xenoliths from the Labait volcano, Tanzania. Geochemistry, Geophysics, Geosystems,

594   16, 1687–1710.

595   Ingrin, J., Hercule, S., and Charton, T. (1995) Diffusion of hydrogen in diopside: Results

596   of dehydration experiments. Journal of Geophysical Research, 100, 15489–15499.

32

597   Ionov, D.A. (1998) Trace element composition of mantle-derived carbonates and

598   coexisting phases in peridotite xenoliths from alkali basalts. Journal of Petrology, 39,

599   1931–1941.

600   Ionov, D.A., Dupuy, C., O'Reilly, S.Y., Kopylova, M.G., and Genshaft, Y.S. (1993)

601   Carbonated peridotite xenoliths from Spitsbergen: implications for trace element

602   signature of mantle carbonate metasomatism. Earth and Planetary Science Letters, 119,

603   283–297.

604   Ionov, D.A., O'Reilly, S.Y., Genshaft, Y.S., and Kopylova, M.G. (1996) Carbonate-

605   bearing mantle peridotite xenoliths from Spitsbergen: phase relationships, mineral

606   compositions and trace-element residence. Contributions to Mineralogy and Petrology,

607   125, 375–392.

608   Ionov, D.A., Griffin, W.L., and O'Reilly, S.Y. (1997) Volatile-bearing minerals and

609   lithophile trace elements in the upper mantle. Chemical Geology, 141, 153–184.

610   Ionov, D.A., Bodinier, J.-L, Mukasa, S.B., and Zanetti, A. (2002a) Mechanisms and

611   sources of mantle metasomatism: Major and trace element compositions of peridotite

612   xenoliths from Spitsbergen in the context of numerical modelling. Journal of Petrology,

613   43, 2219–2259.

614   Ionov, D.A., Mukasa, S.B., and Bodinier, J.-L. (2002b) Sr-Nd-Pb isotopic compositions of

615   peridotite xenoliths from Spitsbergen: Numerical modelling indicates Sr-Nd

33

616   decoupling in the mantle by melt percolation metasomatism. Journal of Petrology, 43,

617   2261–2278.

618 Kendrick, M.A., Jackson, M.G., Kent, A.J.R., Hauri, E.H., Wallace, P.J., and Woodhead,

619   J. (2014) Contrasting behaviours of CO_2, S, H_2O and halogens (F, Cl, Br, and I) in

620   enriched-mantle melts from Pitcairn and Society seamounts. Chemical Geology, 370,

621   69–81.

622 Kendrick, M.A., Jackson, M.G., Hauri, E.H., and Phillips, D. (2015) The halogen (F, Cl,

623   Br, I) and H_2O systematics of Samoan lavas: Assimilated-seawater, EM2 and high-

624     $^3He/^4He$ components. Earth and Planetary Science Letters, 410, 197–209.

625 Khutorskoi, M.D., Leonov, Yu.G., Ermakov, A.V., and Akhmedzyanov, V.R. (2009)

626   Abnormal heat flow and the trough's nature in the Northern Svalbard plate. Doklady

627   Earth Sciences, 424, 29–35.

628 Kilgore, M.L., Peslier, A.H., Brandon, A.D., and Lamb, W.M. (2018) Water and oxygen

629   fugacity in the lithospheric mantle wedge beneath the Northern Canadian Cordillera

630   (Alligator Lake). Geochemistry, Geophysics, Geosystems, 19, 3844–3869, doi:

631   10.1029/2018GC007700.

632 Larsen, C.F., Motyka, R.J., Freymueller, J.T., Echelmeyer, K.A., and Ivins, E.R. (2005)

633   Rapid viscoelastic uplift in southeast Alaska caused by post-Little Ice Age glacial

634   retreat. Earth and Planetary Science Letters, 237, 548–560.

34

635   Lawver, L.A., Müllet, R.D., Srivastava, S.P., and Roest, W. (1990) The opening of the

636   Arctic Ocean. In U. Bleil, and J. Thiede, Eds., Geological History of the Polar Oceans:

637   Arctic Versus Antarctic, pp. 29-62. Kluwer Academic Publisher, Netherlands.

638   Li, Z.A., Lee, C.A., Peslier, A.H., Lenardic, A., and Mackwell, S.J. (2008) Water contents

639   in mantle xenoliths from the Colorado Plateau and vicinity: Implications for the mantle

640   rheology and hydration-induced thinning of continental lithosphere. Journal of

641   Geophysical Research, 113, B09210.

642   Libowitzky, E., and Rossman, G.R. (1996) Principles of quantitative absorbance

643   measurements in anisotropic crystals. Physics and Chemistry of Minerals, 23, 319–327.

644   Liu, Y., Hu, Z., Gao, S., Günther, D., Xu, J., Gao, C., and Chen, H. (2008) In situ analysis

645   of major and trace elements of anhydrous minerals by LA-ICP-MS without applying

646   an internal standard. Chemical Geology, 257, 34–43.

647   Mackwell, S.J., Kohlstedt, D.L., and Paterson, M.S. (1985) The role of water in the

648   deformation of olivine single crystals. Journal of Geophysical Research, 90, 11319–

649   11333.

650   Mei, S., and Kohlstedt, D.L. (2000a) Influence of water on plastic deformation of olivine

651   aggregates: 1. Diffusion creep regime. Journal of Geophysical Research: Solid Earth,

652   105, 21457–21469.

35

653   ——— (2000b) Influence of water on plastic deformation of olivine aggregates: 2.

654   Dislocation creep regime. Journal of Geophysical Research: Solid Earth, 105, 21471–

655   21481.

656   McDonough, W.F. and Sun, S.-S. (1995) The composition of the Earth. Chemical Geology,

657   120, 223–253.

658   Michael, P. (1995) Regionally distinctive sources of depleted MORB: Evidence from trace

659   elements and H_2O. Earth and Planetary Science Letters, 131, 301–320.

660   Miller, G.H., Rossman, G.R., and Harlow, G.E. (1987) The natural occurrence of

661   hydroxide in olivine. Physics and Chemistry of Minerals, 14, 461–472.

662   Mosenfelder, J.L., and Rossman, G.R. (2013a) Analysis of hydrogen and fluorine in

663   pyroxenes: I. Orthopyroxene. American Mineralogist, 98, 1026–1041.

664   ——— (2013b) Analysis of hydrogen and fluorine in pyroxenes: II. Clinopyroxene.

665   American Mineralogist, 98, 1042–1054.

666   Mosenfelder, J.L., Sharp, T.G., Asimow, P.D., and Rossman, G.R. (2006) Hydrogen

667   incorporation in natural mantle olivines. In S.D. Jacobsen, and S. Van Der Lee, Eds.,

668   Earth's Deep Water Cycle, pp. 45–56. American Geophysical Union, Washington, D.

669   C.

670   Niu, Y. (1997) Mantle melting and melt extraction processes beneath ocean ridges:

671   evidence from abyssal peridotites. Journal of Petrology, 38, 1047-1074.

672   Novella, D., Frost, D.J., Hauri, E.H., Bureau, H., Raepsaet, C., and Roberge, M. (2014)

673   The distribution of H_2O between silicate melt and nominally anhydrous peridotite and

674   the onset of hydrous melting in the deep upper mantle. Earth and Planetary Science

675   Letters, 400, 1–13.

676   O'Leary, J.A., Gaetani, G.A., and Hauri, E.H. (2010) The effect of tetrahedral Al^{3+} on the

677   partitioning of water between clinopyroxene and silicate melt. Earth and Planetary

678   Science Letters, 297, 111–120.

679   Pearson, D.G., Canil, D., and Shirey, S.B. (2003) Mantle samples included in volcanic

680   rocks: Xenoliths and diamonds. Treatise on Geochemistry, 2, 171–275.

681   Peslier, A., and Luhr, J. (2006) Hydrogen loss from olivines in mantle xenoliths from

682   Simcoe (USA) and Mexico: Mafic alkalic magma ascent rates and water budget of the

683   sub-continental lithosphere. Earth and Planetary Science Letters, 242, 302–319.

684   Peslier, A.H., and Bizimis, M. (2015) Water in Hawaiian peridotite minerals: A case for a

685   dry metasomatized oceanic mantle lithosphere: Water in Hawaii peridotites.

686   Geochemistry, Geophysics, Geosystems, 16, 1211–1232.

687   Peslier, A.H., Luhr, J.F., and Post, J. (2002) Low water contents in pyroxenes from spinel-

688   peridotites of the oxidized, sub-arc mantle wedge. Earth and Planetary Science Letters,

689   201, 69–86.

690   Peslier, A.H., Woodland, A.B., Bell, D.R., Lazarov, M., and Lapen, T.J. (2012)

691   Metasomatic control of water contents in the Kaapvaal cratonic mantle. Geochimica et

692   Cosmochimica Acta, 97, 213–246.

693   Peslier, A.H., Bizimis, M., and Matney, M. (2015) Water disequilibrium in olivines from

694   Hawaiian peridotites: Recent metasomatism, H diffusion and magma ascent rates.

695   Geochimica et Cosmochimica Acta, 154, 98–117.

696   Peslier, A.H., Schönbächler, M., Busemann, H., and Karato, S.-I. (2017) Water in the

697   Earth's interior: Distribution and origin. Space Science Reviews, 212, 743–810.

698   Plank, T., Cooper, L.B., and Manning, C.E. (2009) Emerging geothermometers for

699   estimating slab surface temperatures. Nature Geoscience, 2, 611–615.

700   Pollitz, F.F., Bürgmann, R. and Romanowicz, B. (1998) Viscosity of oceanic

701   asthenosphere inferred from remote triggering of earthquakes. Science, 280, 1245–

702   1249.

703   Satsukawa, T., Godard, M., Demouchy, S., Michibayashi, K., and Ildefonse, B. (2017)

704   Chemical interactions in the subduction factory: New insights from an in situ trace

705   element and hydrogen study of the Ichinomegata and Oki-Dogo mantle xenoliths

706   (Japan). Geochimica et Cosmochimica Acta, 208, 234–267.

707   Schaffer, L.A., Peslier, A.H., Brandon, A.D., Bizimis, M., Gibler, R., Norman, M., and

708   Harvey, J. (2019) Effects of melting, subduction-related metasomatism, and sub-

709   solidus equilibration on the distribution of water contents in the mantle beneath the Rio

710   Grande Rift. Geochimica et Cosmochimica Acta, 266, 351–381.

711   Shewmon, P. (1989) Diffusion in Solids, second ed. The Minerals, Metals and Materials

712   Society, Warrendale, PA.

713   Skogby, H., Bell, D.R., and Rossman, G.R. (1990) Hydroxide in pyroxene: Variations in

714   the natural environment. American Mineralogist, 75, 764–774.

715   Stalder, R., and Skogby, H. (2003) Hydrogen diffusion in natural and synthetic

716   orthopyroxene. Physics and Chemistry of Minerals, 30, 12–19.

717   Soustelle, V., Tommasi, A., Demouchy, S., and Ionov, D.A. (2010) Deformation and fluid-

718   rock interaction in the supra-subduction mantle: Microstructures and water contents in

719   peridotite xenoliths from the Avacha volcano, Kamchatka. Journal of Petrology, 51,

720   363-394.

721   Sun, S. -S., and McDonough, W.F. (1989) Chemical and isotopic systematics of oceanic

722   basalts: Implications for mantle composition and processes. Geological Society,

723   London, Special Publications, 42, 313–345.

724   Sundvall, R., and Stalder, R. (2011) Water in upper mantle pyroxene megacrysts and

725   xenocrysts: A survey study. American Mineralogist, 96, 1215–1227.

726   Sushchevskaya, N.M., Evdokimov, A.N., Belyatsky, B.V., Maslov, V.A., and Kuz'min,

727   D.V. (2008) Conditions of Quaternary magmatism at Spitsbergen Island.

728   Geochemistry International, 46, 1–16.

729   Tenner, T.J., Hirschmann, M.M., Withers, A.C., and Hervig, R.L. (2009) Hydrogen

730   partitioning between nominally anhydrous upper mantle minerals and melt between 3

731   and 5 GPa and applications to hydrous peridotite partial melting. Chemical Geology,

732   262, 42–56.

733   Vågnes, E., and Amundsen, H.E.F. (1993) Late Cenozoic uplift and volcanism on

734   Spitsbergen: Caused by mantle convection? Geology, 21, 251–253.

735   Wallace, P.J. (2002) Volatiles in submarine basaltic glasses from the Northern Kerguelen

736   Plateau (ODP Site 1140): Implications for source region compositions, magmatic

737   processes, and plateau subsidence. Journal of Petrology, 43, 1311–1326.

738   Walter, M.J. (2003). Melt extraction and compositional variability in mantle lithosphere.

739   Treatise on Geochemistry, 2, 363–394.

740   Wang, D., Mookherjee, M., Xu, Y., and Karato, S. (2006) The effect of water on the

741   electrical conductivity of olivine. Nature, 443, 977–980.

742   Withers, A.C., Bureau H., Raepsaet C. and Hirschmann M.M. (2012) Calibration of

743   infrared spectroscopy by elastic recoil detection analysis of H in synthetic olivine.

744   Chemical Geology, 334, 92–98.

40

745   Workman, R.K., Hauri, E., Hart, S.R., Wang, J., and Blusztajn, J. (2006) Volatile and trace

746   elements in basaltic glasses from Samoa: Implications for water distribution in the

747   mantle. Earth and Planetary Science Letters, 241, 932–951.

748   Xu, Y., Tang, W., Hui, H., Rudnick, R.L., Shang, S., and Zhang, Z. (2019) Reconciling the

749   discrepancy between the dehydration rates in mantle olivine and pyroxene during

750   xenolith emplacement. Geochimica et Cosmochimica Acta, 267, 179–195.

751   Yoshino, T., Matsuzaki, T., Yamashita, S., and Katsura, T. (2006) Hydrous olivine unable

752   to account for conductivity anomaly at the top of the asthenosphere. Nature, 443, 973–

753   976.

754   Zhang, H., Zheng, J., Lu, J., Pan, S., Zhao, Y., Lin, A., and Xiang, L. (2018) Composition

755   and evolution of the lithospheric mantle beneath the interior of the South China Block

756   insights from trace elements and water contents of peridotite xenoliths. Contributions

757   to Mineralogy and Petrology. 173, 53, doi:10.1007/s00410-018-1476-z.

758

41

759 **Figure caption**

760 **Figure 1.** Representative polarized FTIR spectra normalized to 1 cm thickness for (a)

761 olivine in peridotite xenolith, (b) olivine in wehrlite xenolith, (c) orthopyroxene, and (d)

762 clinopyroxene from Spitsbergen mantle xenoliths. Spectra for three perpendicular

763 orientations (α, β, and γ) are shifted vertically for comparison. The O-H bands of olivine

764 can be separated into two groups based on the wavenumber (Bai and Kohlstedt 1993).

765

766 **Figure 2.** O-H absorbance profiles in olivine from sample 4-36-90. (a) Plane-polarized

767 light optical image of olivine showing the locations (the red solid line AB) of FTIR

768 analyses. (b) Integrated Group I O-H absorbances with diffusion modeling results obtained

769 using diffusivity equations (Xu et al. 2019). (c) Integrated Group II O-H absorbances

770 obtained along the profile shown in (a). The diffusion temperature used in the model is the

771 equilibrium temperature (950 °C; Table 1). The calculated diffusion time is 0.4 hours. The

772 vertical error bars represent the uncertainty on the absorbance being 15 % and the

773 horizontal ones are 25 μm based on the aperture size.

774

775 **Figure 3.** O-H absorbance profiles in (a) olivine, (b) orthopyroxene, and (c) clinopyroxene

776 from sample 318-1. (a1, b1, c1) Plane-polarized light optical images showing the locations

777 (the red solid lines AB) of FTIR analyses. (a2, b2, c2) Integrated O-H absorbances with

42

778   diffusion modeling results obtained along the profiles shown in (a1, b1, c1). The diffusion

779   temperature used in the modeling was estimated to be 750 °C with $D_H^{Ol/Opx} = 1.4$ and

780    $D_H^{Ol/Cpx} = 0.7$ (Xu et al. 2019). The uncertainty on the absorbance is 15 % (vertical error

781   bar) and on the distance is 25 μm (horizontal error bar).

782

783   **Figure 4.** Trace-element compositions of Spitsbergen xenolithic clinopyroxenes. (a) and

784   (b) Comparison of trace-element abundances in clinopyroxene from xenolith 318-1

785   measured in the present study and by Ionov et al. (2002a). Primitive-mantle (PM)

786   normalized REE distribution patterns for clinopyroxene in (c) Type-1 and (d) Type-2

787   xenoliths. Primitive mantle values are from McDonough and Sun (1995). REE data (gray

788   symbols) for xenoliths which trace elements were measured by Ionov et al. (2002a) are

789   shown for comparison.

790

791   **Figure 5.** Comparison of hydrogen distributions (a) between olivine and orthopyroxene,

792   (b) between olivine and clinopyroxene, (c) between orthopyroxene and clinopyroxene. The

793   solidus hydrogen concentrations (Table 4) are also plotted for comparison. The gray lines

794   represent experimentally determined partition coefficients of hydrogen between olivine

795   and pyroxenes (Hauri et al. 2006; Tenner et al. 2009; Novella et al. 2014; Demouchy et al.

43

796   2017). Error bars represent the 2σ uncertainty. H06, Hauri et al. (2006); T09, Tenner et al.

797   (2009); N14, Novella et al. (2014); D17, Demouchy et al. (2017).

798

799   **Figure 6.** Hydrogen contents of Spitsbergen (a) olivine, (b) orthopyroxene, and (c)

800   clinopyroxene versus equilibrium temperature. The equilibrium temperatures were

801   calculated using a Ca-in-Opx thermometry (Brey and Köhler 1990) at 1.5 GPa (Table 1).

802   The dashed lines represent linear regressions of Type-1 and Type-2 data to show

803   correlations between equilibrium temperature and hydrogen content in mineral. Error bars

804   represent the 2σ uncertainty.

805

806   **Figure 7.** Hydrogen contents of Spitsbergen (a) olivine, (b) orthopyroxene, and (c)

807   clinopyroxene versus (1) forsterite content, (2) spinel Cr#, (3) whole-rock Al_2O_3 content,

808   and (4) clinopyroxene Yb content. Major and trace element data are from Ionov et al.

809   (2002a). Error bars represent the 2σ uncertainty. Fo, forsterite content; WR, whole rock.

810

811   **Figure 8.** Hydrogen contents of Spitsbergen (a) olivine, (b) orthopyroxene, and (c)

812   clinopyroxene versus (1) La content, (2) Th content, and (3) primitive-mantle normalized

813   La/Yb in clinopyroxene. Trace-element data are from Ionov et al. (2002a), with the

814   exception of data for xenoliths 318-1, 43-86, 28b, and 39-86-1, which were obtained in the

44

815   present study. The dashed lines represent linear regression of the Type-1 data and show the

816   correlation between clinopyroxene LREE contents and hydrogen contents in NAMs.

817

818   **Figure 9.** Hydrogen contents of minerals in Spitsbergen mantle xenoliths: (a) olivine, (b)

819   orthopyroxene, and (c) clinopyroxene versus (1) whole-rock Nb content, (2) Th content,

820   and (3) primitive-mantle normalized Zr/Hf. The whole-rock trace element data are from

821   Ionov et al. (2002a). The dashed lines represent linear regression of the Type-1 data

822   excluding xenolith 39-86-1. This excluded sample is chemically heterogeneous and thus

823   its bulk compositions may not be representative (Ionov et al., 2002a).

824

825   **Figure 10.** Hydrogen contents of Spitsbergen (a) olivine, (b) orthopyroxene, and (c)

826   clinopyroxene versus (1) Sr and (2) Nd isotope compositions in clinopyroxene. Isotope

827   data are from Ionov et al. (2002b). The dashed lines represent linear regression of the Type-

828   1 data excluding labeled data points.

829

830   **Figure 11.** Hydrogen contents of Spitsbergen (a) olivine, (b) orthopyroxene, and (c)

831   clinopyroxene versus (1) clinopyroxene Nb and (2) whole-rock Nb. The data for Nb

832   contents are from Ionov et al. (2002a). The Nb abundances in Type-1 clinopyroxenes were

833   too low to be determined accurately.

45

834

835   **Figure 12.** H_2O/Ce and H_2O/La ratios of melts in equilibrium with clinopyroxenes versus

836   clinopyroxene isotopic data. (a) Comparison of H_2O/Ce ratios of melts in equilibrium with

837   Type-2 clinopyroxenes and those of MORB (Michael 1995), OIB (Dixon and Clague 2001;

838   Dixon et al. 2002; Wallace 2002; Workman et al. 2006; Cabral et al. 2014; Kendrick et al.

839   2014, 2015; Bizimis and Peslier 2015), and arc lava (Plank et al. 2009). (b), (c), (d) Mixing

840   models for clinopyroxene isotope compositions and melt H_2O/Ce or H_2O/La ratios. The

841   dashed line represents the mixing line excluding heterogeneous sample 39-86-1. Sample

842   39-86-2 represents the depleted end-member: $^{87}Sr/^{86}Sr = 0.7025$, $^{143}Nd/^{144}Nd = 0.5136$,

843    $H_2O/Ce = 1010$, and $H_2O/La = 664$. The average value of Type-2 samples represents the

844   enriched end-member: $^{87}Sr/^{86}Sr = 0.704$, $^{143}Nd/^{144}Nd = 0.5128$, $H_2O/Ce = 147$, and H_2O/La

845    $= 180$. Isotope data are from Ionov et al. (2002b).

846

847   **Figure 13**. Bulk-rock hydrogen content versus calculated effective viscosity. The pink area

848   represents the viscosity range of global asthenosphere (2.7×10^{17}–2×10^{19} Pa·s; Craig and

849   McKenzie 1986; Hager 1991; Pollitz et al. 1998; Larson et al. 2005). The solidus

850   temperature is assumed to be 1350 °C, the temperature of Spitsbergen asthenosphere

851   (Vågnes and Amundsen 1993). Bulk-rock hydrogen contents of Spitsbergen xenoliths are

852   listed in Table 4.

46

853   **Table 1.** Summary of Spitsbergen mantle xenoliths analyzed in this study

Sample	Locality	Lithology[a,d]	Texture[a,d]	Modal mineralogy[a,d]	T (°C)[b]	Mg#[a]	Cr#[a]
Type-1							
4-25-90	Halvdan	Spl Lherzolite	Crs to Mos-Eq	$Ol_{74.0}Opx_{13.2}Cpx_{10.1}Spl_{2.7}$	1000	0.910	0.204
4-36-90	Halvdan	Spl Lherzolite	Crs to Mos-Eq	$Ol_{75.4}Opx_{11.3}Cpx_{10.6}Spl_{2.8}$	950	0.906	0.170
315-6	Halvdan	Spl Lherzolite	Crs to Prb	$Ol_{60.4}Opx_{25.5}Cpx_{9.8}Spl_{1.7}Amph_{2.4}$	890	0.904	0.124
28b	Sverre	Spl Lherzolite	Crs to Mos-Prb	$Ol_{63.6}Opx_{27.4}Cpx_{7.5}Spl_{1.5}$	940	0.905	0.133
39-86-2	Sverre	Spl Lherzolite	Crs to Mos-Prb	$Ol_{68.2}Opx_{17.3}Cpx_{11.3}Spl_{3.2}$	930	0.905	0.125
63-90-18	Sverre	Spl Lherzolite	Crs to Mos-Prb	$Ol_{59.4}Opx_{28.6}Cpx_{10.1}Spl_{1.8}$	900	0.901	0.136
39-86-1	Sverre	Spl Lherzolite	Crs to Mos-Prb	$Ol_{69.5}Opx_{18.2}Cpx_{10.0}Spl_{2.3}$	887	0.906	0.135
Type-2							
318	Halvdan	Spl Harzburgite	Mos-Prb	$Ol_{79.4}Opx_{12.3}Cpx_{3.0}Spl_{1.1}Amph_{4.2}$	930	0.915	0.253
318-1	Halvdan	Spl Lherzolite	Crs	$Ol_{60.2}Opx_{25.1}Cpx_{12.1}Spl_{1.6}Amph_{1.0}$	1025	0.908	0.164
4-90-9	Halvdan	Spl Lherzolite	Crs to Mos-Eq	Ol, Opx, Cpx, Spl, Amph	990	0.897	0.162
43-86[c]	Sverre	Spl Lherzolite	Crs to Mos-Prb	Ol, Opx, Cpx, Spl, Ap, Pl	915	0.911	0.213
Other							
26a	Sverre	Spl Harzburgite	Crs-Prb	$Ol_{69.6}Opx_{26.5}Cpx_{2.9}Spl_{1.0}$	1000	0.912	0.416
4a-90-1(vein)	Sigurd	Amph Wehrlite		Ol, Cpx, Amph, Phl		0.890	

854   *Note*: [a] Lithology, texture, modal mineralogy, Mg# in olivine, and Cr# in spinel of all samples except sample 43-86 are from Ionov et al. (1996,
855   2002a).
856   [b] Except sample 43-86, equilibrium temperatures (T) of all samples (grain core) calculated using Ca-in-Opx thermometry (Brey and Köhler 1990)
857   at 1.5 GPa, are from Ionov et al. (2002a).
858   [c] All data for sample 43-86 are from Ionov et al. (1993, 1996).
859   [d] Crs, coarse; Mos, mosaic; Eqg, equigranular; Prb, porphyroblastic; Ol, olivine; Opx, orthopyroxene; Cpx, clinopyroxene; Spl, spinel; Amph,
860   amphibole; Ap, apatite; Pl, plagioclase; Phl, phlogopite.

861 **Table 2.** Polarized integrated O-H absorbances and hydrogen contents of olivine, orthopyroxene, and clinopyroxene in Spitsbergen mantle
862 xenoliths

	Olivine[a]								Orthopyroxene[a]				Clinopyroxene[a]			
	A_α		A_β		A_γ		H_2O^b	H_2O^c	A_α	A_β	A_γ	H_2O^d	A_α	A_β	A_γ	H_2O^d
	Group I	Group II	Group I	Group II	Group I	Group II										
Sample	(cm^{-2})	(cm^{-2})	(cm^{-2})	(cm^{-2})	(cm^{-2})	(cm^{-2})	(ppm)	(ppm)	(cm^{-2})	(cm^{-2})	(cm^{-2})	(ppm)	(cm^{-2})	(cm^{-2})	(cm^{-2})	(ppm)
							Type-1									
4-25-90	1.4	2	4.4	8.8	22.5	1.8	6.3±0.8(4)	4.0±0.4	1083	1146	2077	290±25(4)	1398	1217	1093	520±54(5)
4-36-90	1.3	3	3.7	15	18	3	6±1(5)	3.8±0.6	964	994	1758	250±22(5)	1327	1135	971	480±49(5)
315-6	0	2.9	2.3	19	10.5	3.1	4.4±0.8(4)	2.8±0.5	786	841	1330	200±20(5)	1209	1125[e]	819	450±57(4)
28b	1.1	2.2	3.9	13.7	16.2	2.1	5.4±0.6(5)	3.4±0.3	702[e]	735	1029	170±17(3)	1031	1046	686	390±36(6)
39-86-2	0	1.9	1.6	7.6	7.7	2.1	2.7±0.3(5)	1.7±0.1	479	537	1100	140±17(5)	878	924	741	360±38(3)
63-90-18	0	2.3	2.4	13	9	2.4	3.5±0.9(6)	2.2±0.6	517	630	973	140±12(6)	1021	848	764	370±40(5)
39-86-1	0	2.1	2.1	11.5	9.1	2.1	3.3±0.3(5)	2.1±0.2	533	637	1006	150±13(4)	970	811	694	350±37(6)
							Type-2									
318	0	2.0	1.1	16	4.2	2.1	2.6±0.4(6)	1.6±0.2	612	620	1090	160±17(7)	915	901	670	350±45(3)
318-1	2.0	5.3	5.4	35	27	3.7	10±2(5)	6±1	1122	1142	2052	290±25(5)	1360	1380	1200	560±65(4)
4-90-9	0	4.3	4.6	19	22.5	3.4	7.2±0.8(5)	4.6±0.4	889	927	1714	240±20(4)	1151	1128	939	450±48(5)
43-86	0	3.0	1.2	18	5.3	2.8	3.1±0.6(6)	2.0±0.4	507	546	1008	140±11(5)	924	802	732	350±32(5)
							Other									
26a	0	0	0.9	5	2.1	1.5	1.1±0.2(6)	0.7±0.1	502	405	996	130±16(6)	-	-	-	-
4a-90-1	0	0	3.0	4.2	17.2	-	4.1±0.5(6)	2.6±0.3					-	-	-	-

863 *Note*: [a] Numbers in parentheses are the number of grains analyzed for each type of mineral.

48

864   [b] Olivine hydrogen contents were calculated with the following integral specific absorption coefficients: 5.32 $ppm^{-1} \cdot cm^{-2}$ for Group I O-H bands

865   and 5.32×2.4 $ppm^{-1} \cdot cm^{-2}$ for Group II O-H bands (Bell et al. 2003).

866   [c] Olivine hydrogen contents were calculated with the following integral specific absorption coefficients: 8.40 $ppm^{-1} \cdot cm^{-2}$ for Group I O-H bands

867   (Withers et al. 2012) and 8.40×2.4 $ppm^{-1} \cdot cm^{-2}$ for Group II O-H bands (Bell et al. 2003; Withers et al. 2012).

868   [d] Orthopyroxene and clinopyroxene hydrogen contents were calculated with the following integral specific absorption coefficients: 14.84±0.59

869    $ppm^{-1} \cdot cm^{-2}$ for orthopyroxene and 7.09±0.32 $ppm^{-1} \cdot cm^{-2}$ for clinopyroxene (Bell et al. 1995).

870   [e] A_α or A_β that was absent in the mineral mount was estimated based on the A_α/A_β from other samples.

871 **Table 3.** Trace-element compositions of clinopyroxene in Spitsbergen mantle
872 xenoliths

Sample	28b		39-86-1		43-86		318-1		BCR-2G		BCR-2Gᵃ
	ppm	1σ	ppm	1σ	ppm	1σ	ppm	1σ	ppm	1σ	ppm
Li	1.2	0.2	1.6	0.3	1.0	0.2	1.2	0.2	9.3	0.8	9
Sc	69	2	68	3	75	3	58	2	34	2	33
Ti	2400	79	2830	97	1240	44	1660	61	12400	530	14100
V	284	8	280	9	240	7	241	8	430	19	425
Cr	6000	195	4500	140	5600	170	7700	240	19	3	17
Co	20	1	19	1	18	1	22	1	37	2	38
Ni	330	11	320	10	310	10	355	11	13	1	13
Cu	0.8	0.2	1.3	0.2	0.6	0.1	1.4	0.2	17	1	21
Zn	10	2	7	1	7	1	10	1	130	8	125
Ga	2.8	0.2	3.0	0.2	2.5	0.2	3.8	0.3	22	1	23
Sr	160	5	64	2	320	10	374	13	350	16	342
Y	16.2	0.7	19.9	0.8	13.2	0.6	14.6	0.7	34	2	35
Zr	29	1	32	1	26	1	18	1	183	8	184
Nb					0.06	0.02	0.80	0.08	11.8	0.6	12.5
La	8.7	0.3	2.0	0.1	17.9	0.6	11.3	0.4	24	1	24.7
Ce	13.3	0.5	4.0	0.2	43	1	29	1	52	2	53
Pr	1.12	0.07	0.67	0.05	4.8	0.2	3.8	0.2	6.5	0.3	6.7
Nd	4.2	0.3	3.7	0.3	14.9	0.7	14.1	0.7	28	2	29
Sm	1.5	0.2	1.8	0.2	2.1	0.2	2.7	0.2	7.3	0.4	6.6
Eu	0.62	0.06	0.69	0.06	0.73	0.06	0.96	0.08	2.0	0.1	2.0
Gd	2.4	0.2	2.8	0.2	2.2	0.2	2.7	0.2	7.7	0.5	6.7
Tb	0.43	0.03	0.50	0.04	0.35	0.03	0.42	0.03	0.98	0.06	1.02
Dy	2.9	0.2	3.7	0.2	2.4	0.2	2.7	0.2	6.5	0.4	6.4
Ho	0.63	0.04	0.79	0.05	0.52	0.04	0.60	0.04	1.26	0.08	1.27
Er	1.9	0.1	2.4	0.2	1.6	0.1	1.8	0.1	3.8	0.2	3.7
Tm	0.26	0.02	0.34	0.03	0.22	0.02	0.24	0.02	0.58	0.04	0.51
Yb	1.7	0.2	2.2	0.2	1.5	0.1	1.6	0.2	3.5	0.3	3.4
Lu	0.25	0.02	0.31	0.03	0.22	0.02	0.23	0.02	0.48	0.03	0.50
Hf	1.0	0.1	1.1	0.1	0.60	0.06	0.63	0.06	5.2	0.3	4.8
Ta	0.009	0.004		0.002		0.003	0.020	0.006	0.80	0.05	0.8
Pb	0.73	0.06	0.19	0.03	0.87	0.06	0.29	0.03	11.1	0.5	
Th	1.22	0.06	0.22	0.02	1.80	0.08	0.59	0.04	5.9	0.3	5.9
U	0.32	0.03	0.07	0.01	0.43	0.03	0.10	0.01	1.79	0.08	1.7

873 *Note:* ᵃ The preferred values of trace-element compositions for reference standard BCR-
874 2G are from the GeoReM database [http://georem.mpch-mainz.gwdg.de/], United
875 States Geological Survey Preliminary Report (1996) 1-10].
876

50

877 **Table 4.** Hydrogen diffusivities, bulk-rock and solidus hydrogen contents, partition coefficients, effective viscosity of Spitsbergen xenoliths

Sample	D_H[a]			Solidus H_2O			K_H[b]	K_{Ce}[c]	η_{eff}[d]	Bulk-rock H_2O[e]	
	Olivine	Orthopyroxene	Clinopyroxene	Olivine	Orthopyroxene	Clinopyroxene	Clinopyroxene/melt	Clinopyroxene/melt	Pa·s	ppm	2σ
Type-1											
4-25-90	3.4E-13	2.0E-13		22	373	404	0.010	0.130	2.3E+23	93	6
4-36-90	4.5E-12			21	333	360	0.010	0.128	1.6E+24	86	6
315-6	1.7E-12			17	288	312	0.009	0.132	2.9E+25	98	8
28b	3.9E-12			18	248	268	0.010	0.136	2.8E+24	79	5
39-86-2				12	216	233	0.010	0.129	1.2E+25	67	5
63-90-18	2.1E-12			14	219	237	0.010	0.135	2.7E+25	80	5
39-86-1	1.7E-12			13	220	238	0.010	0.134	5.2E+25	65	4
Type-2											
318	3.3E-12			12	228	246	0.009	0.125	1.3E+25	32	3
318-1	1.2E-13	8.8E-14	1.6E-13	29	387	419	0.012	0.132	5.1E+22	150	10
4-90-9	8.1E-12			22	316	342	0.011	0.131	2.8E+23		
43-86	6.4E-13		3.1E-13	13	213	230	0.009	0.123	1.8E+25		
Other											
26a	5.1E-13	2.7E-13					0.007	0.121	5.3E+24	35	4
4a-90-1(vein)							0.011	0.145			

878 *Note:* [a] Diffusivities of hydrogen (D_H) in olivine and pyroxene were calculated using Equations 3-5 in Xu et al. (2019).

879 [b] Partition coefficients of hydrogen between clinopyroxene and melt ($K_H^{Cpx/melt} = C_H^{Cpx}/C_H^{melt}$) were calculated using Equation (10) in O'Leary

880 et al. (2010).

881   [c] Partition coefficients of Ce between clinopyroxene and melt ($K_{Ce}^{Cpx/melt} = C_{Ce}^{Cpx}/C_{Ce}^{melt}$) were calculated using Equation (298) in Bédard

882   (2014).

883   [d] Effective viscosity (η_{eff}) was calculated following the method of Li et al. (2008).

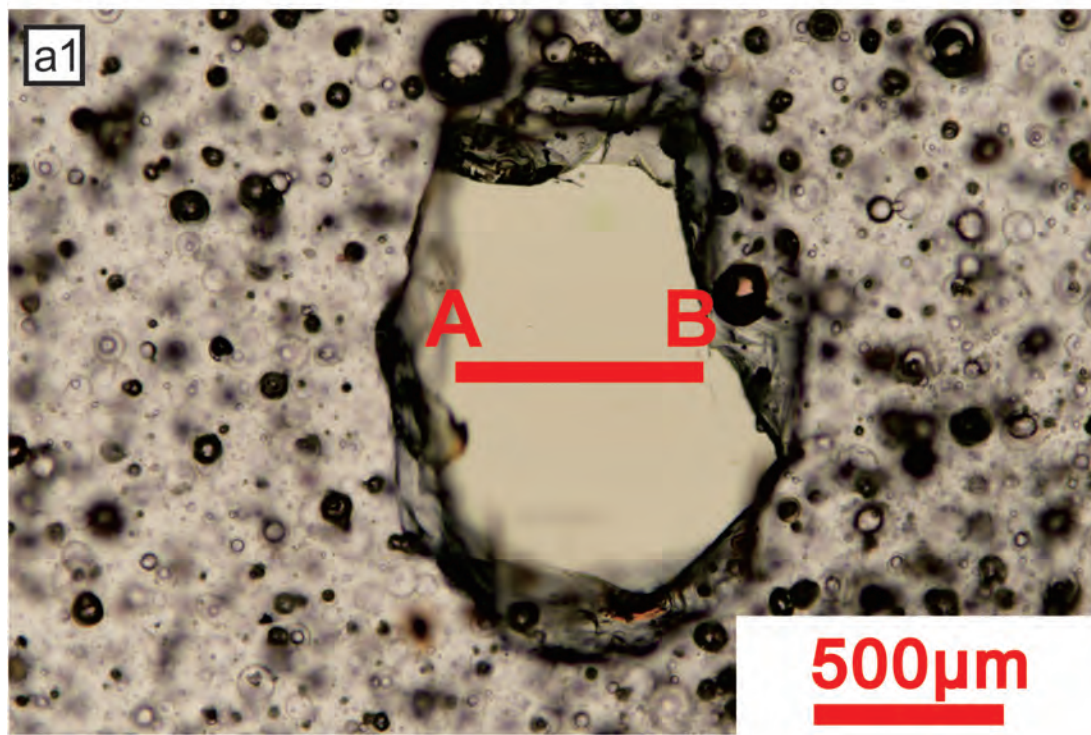884   [e] Amphibole was not considered in the calculation of bulk-rock hydrogen content.

52
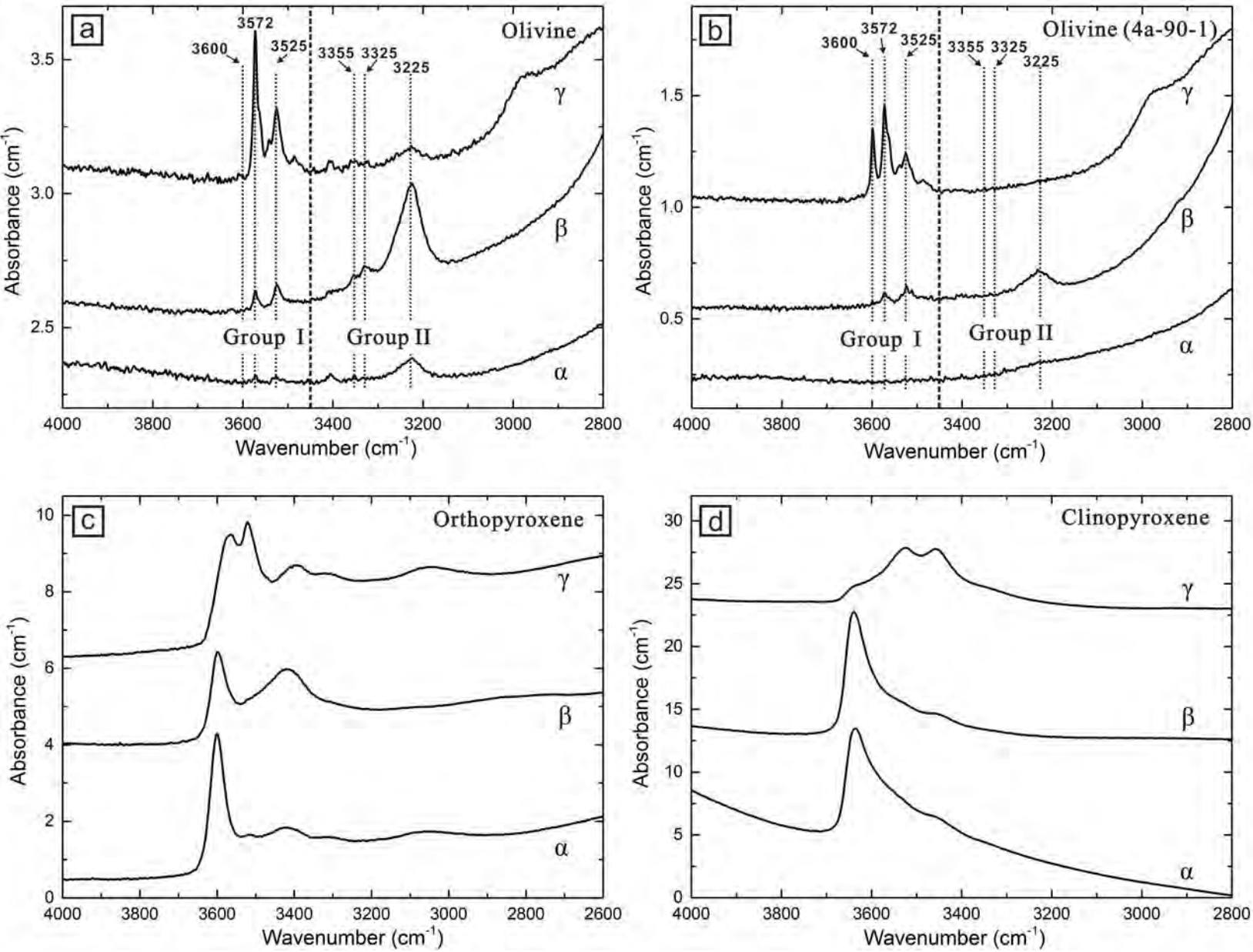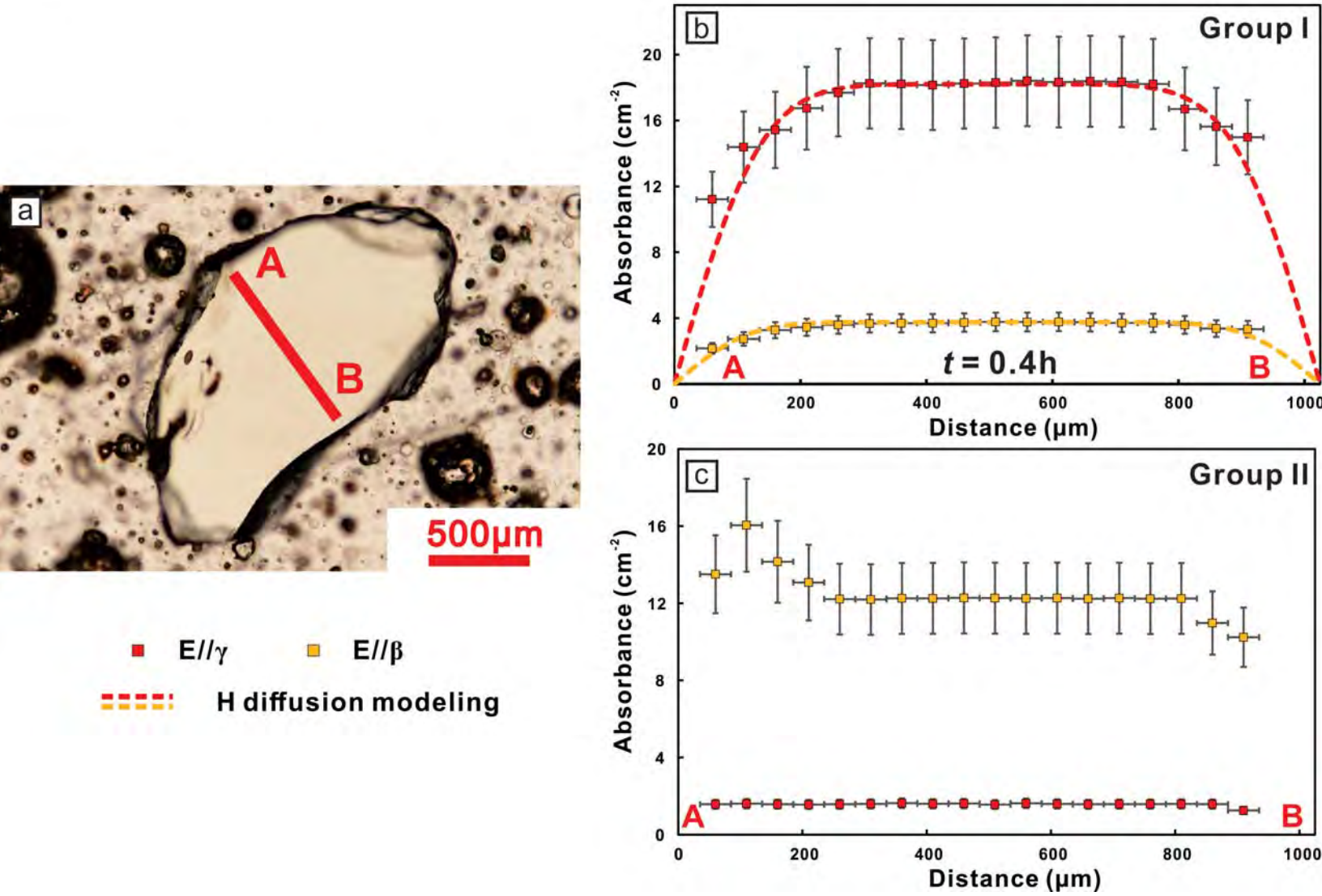
Figure 1

Figure 2

Figure 3
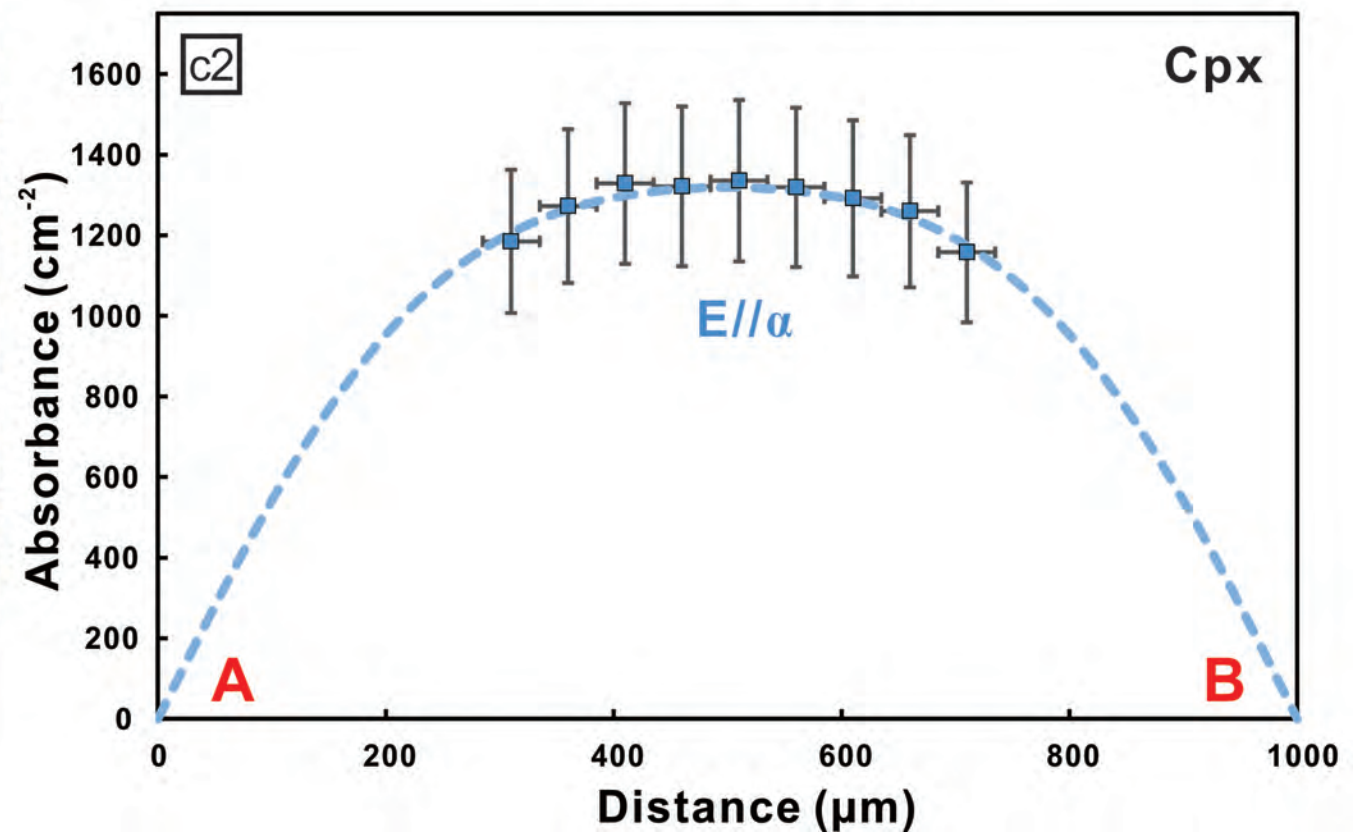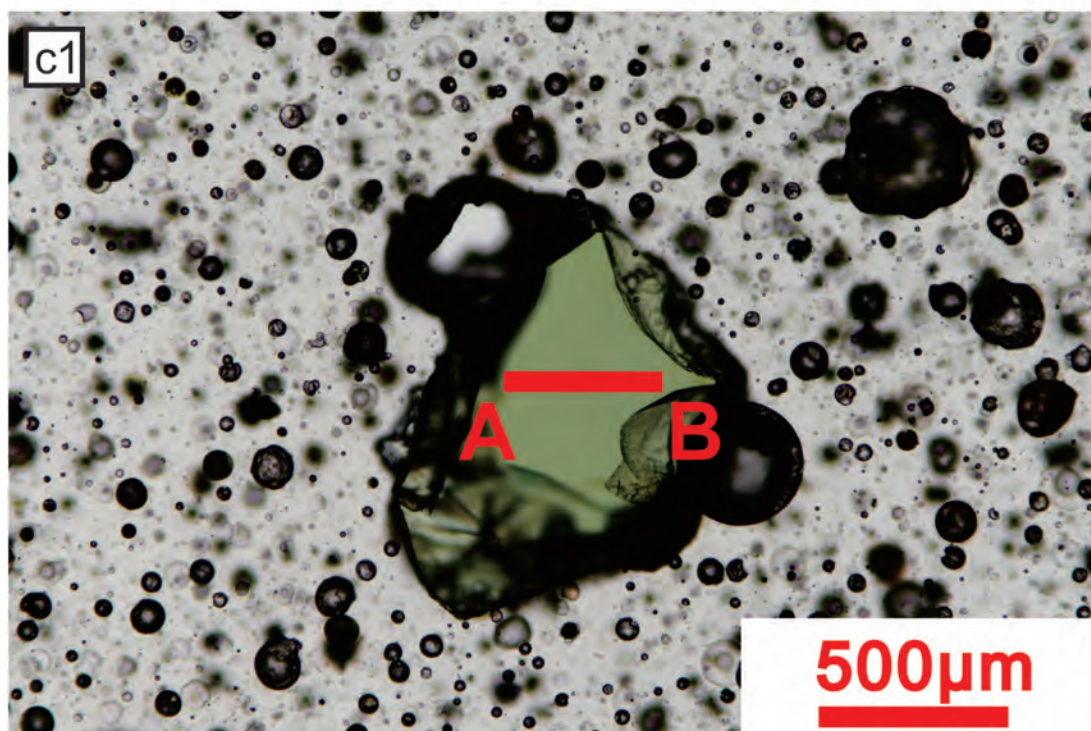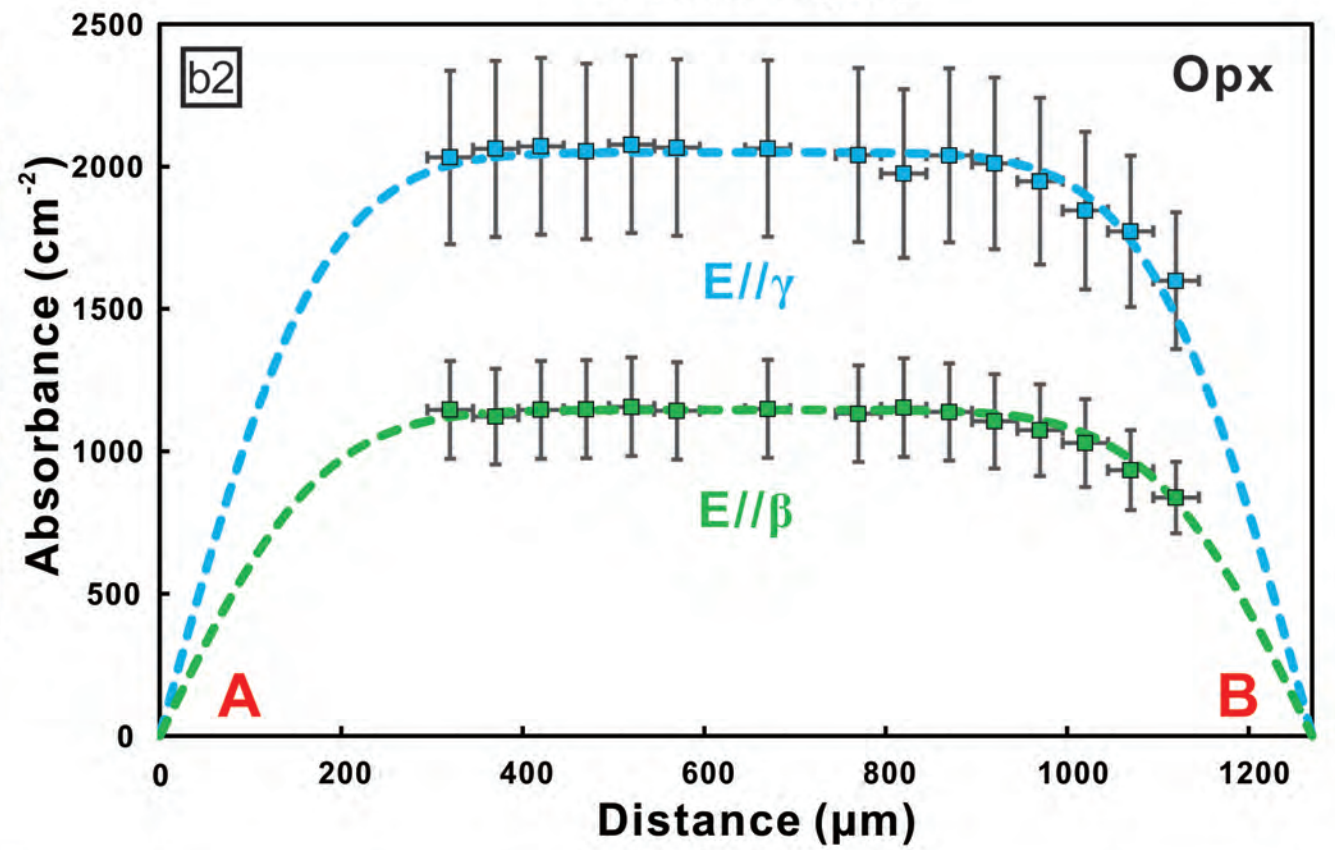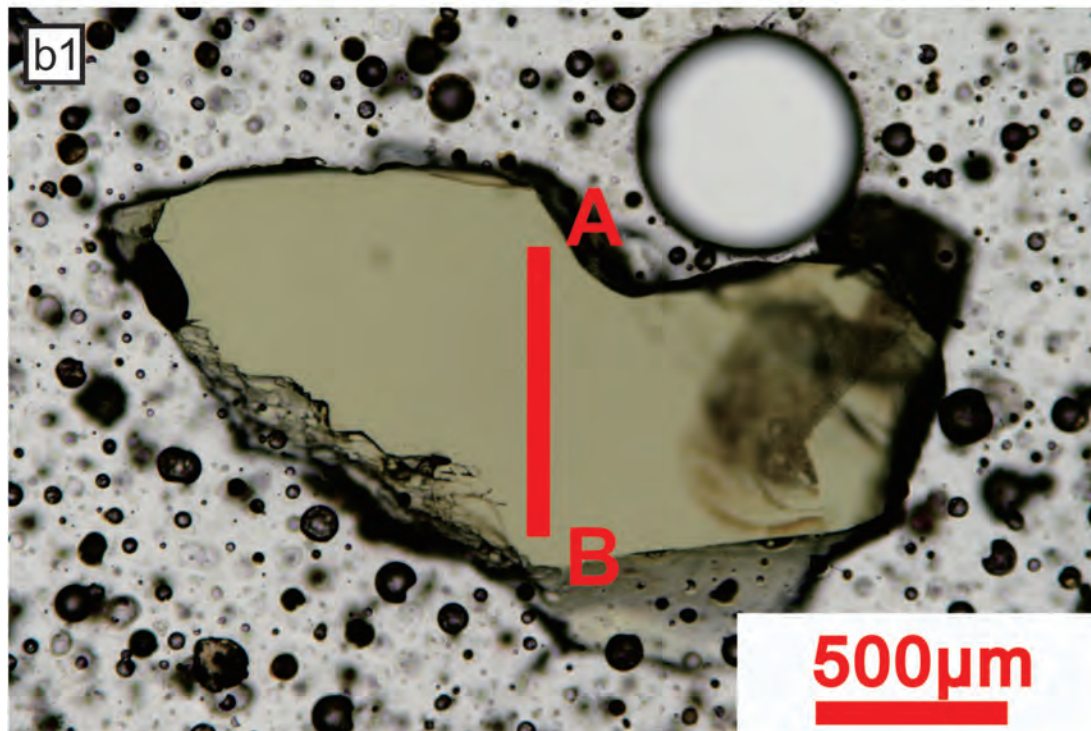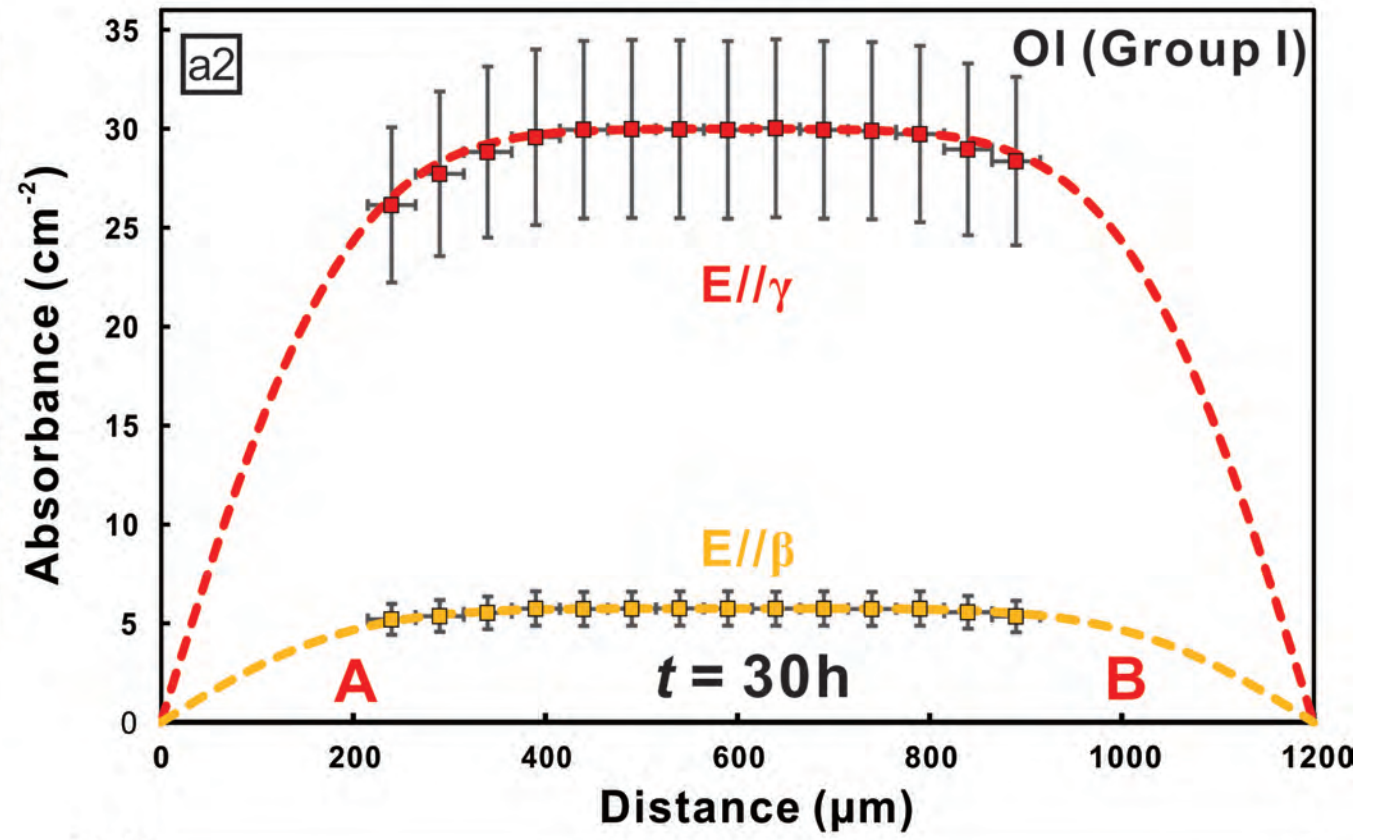
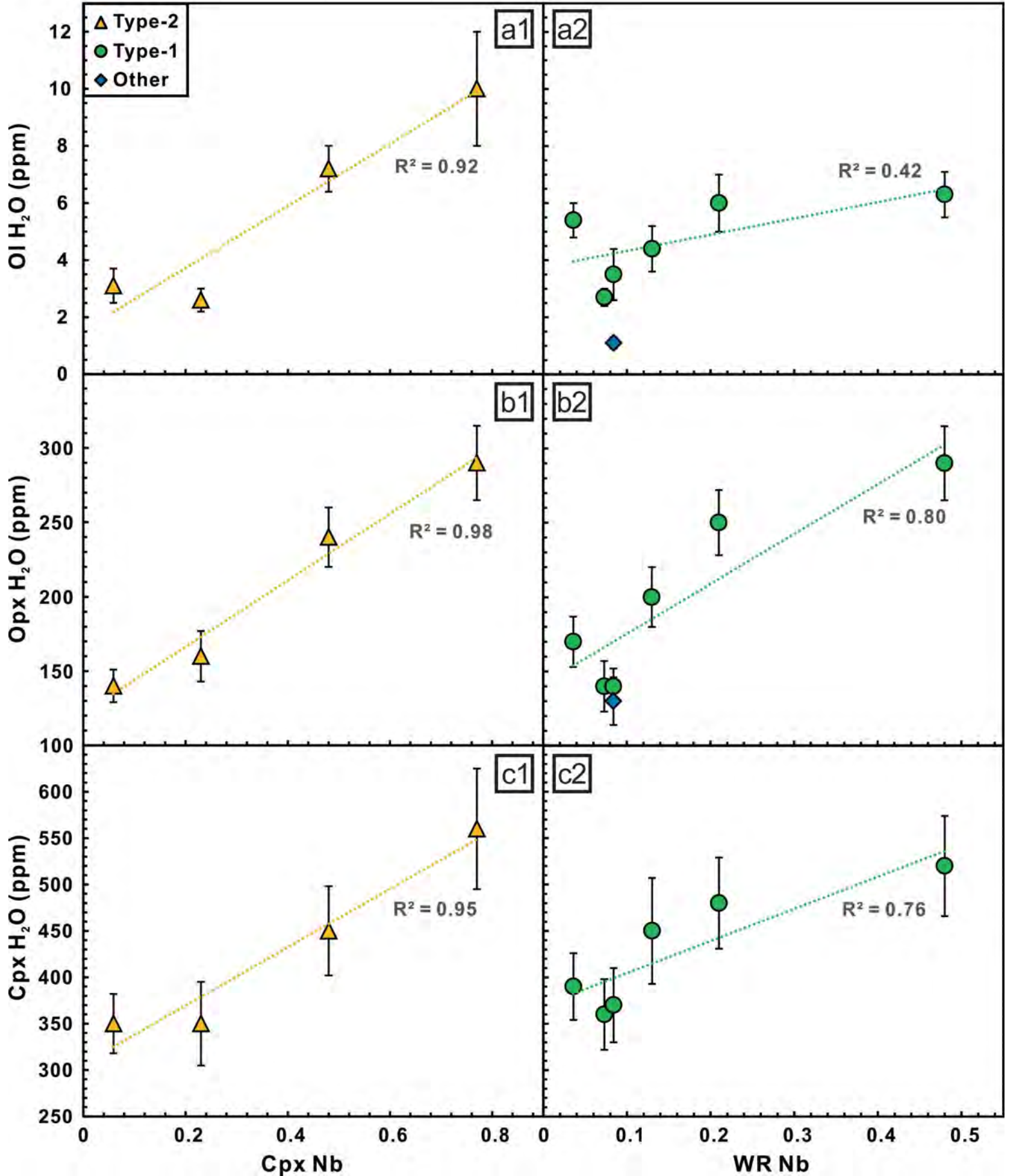# Figure 4
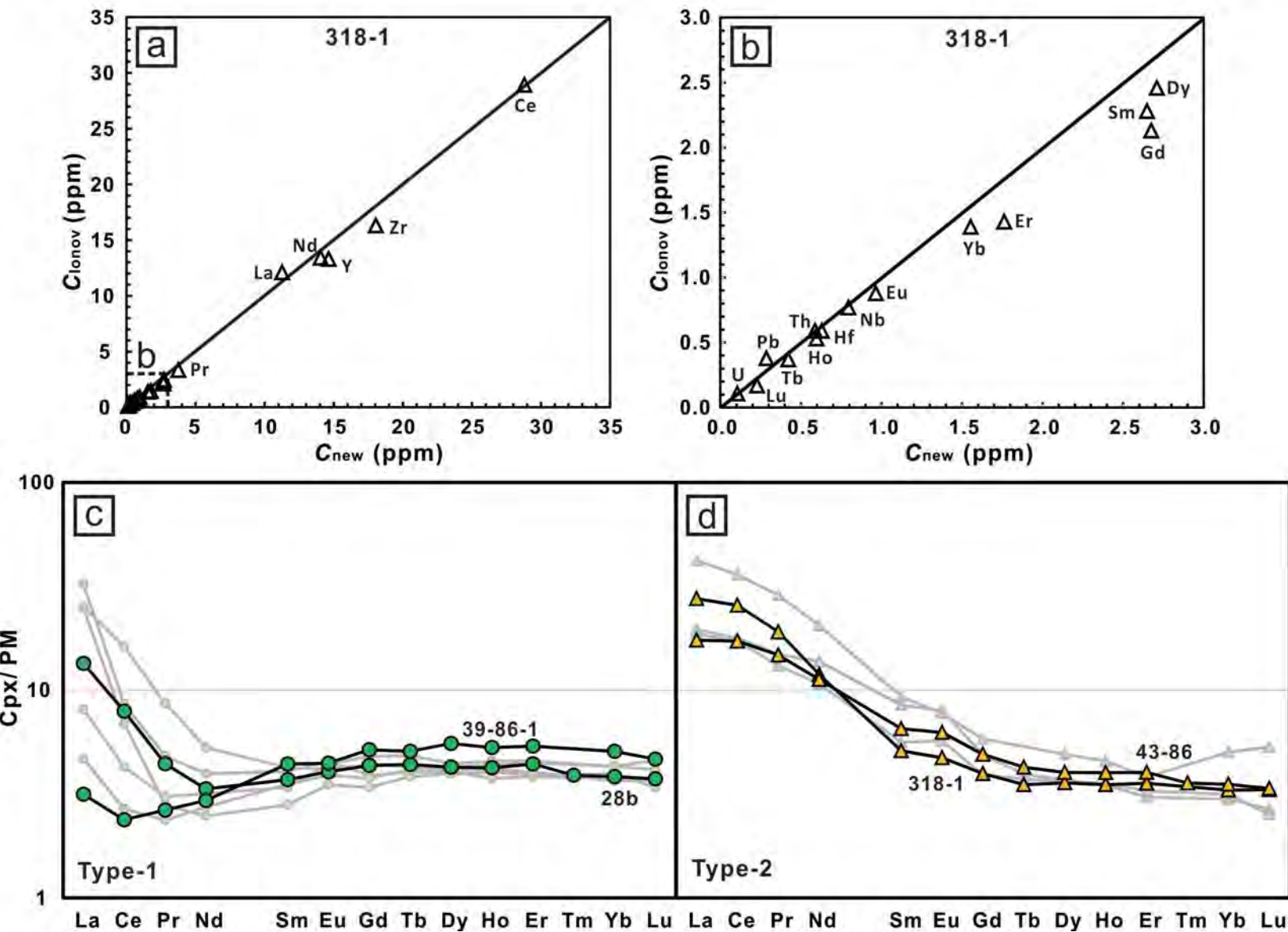
Figure 5
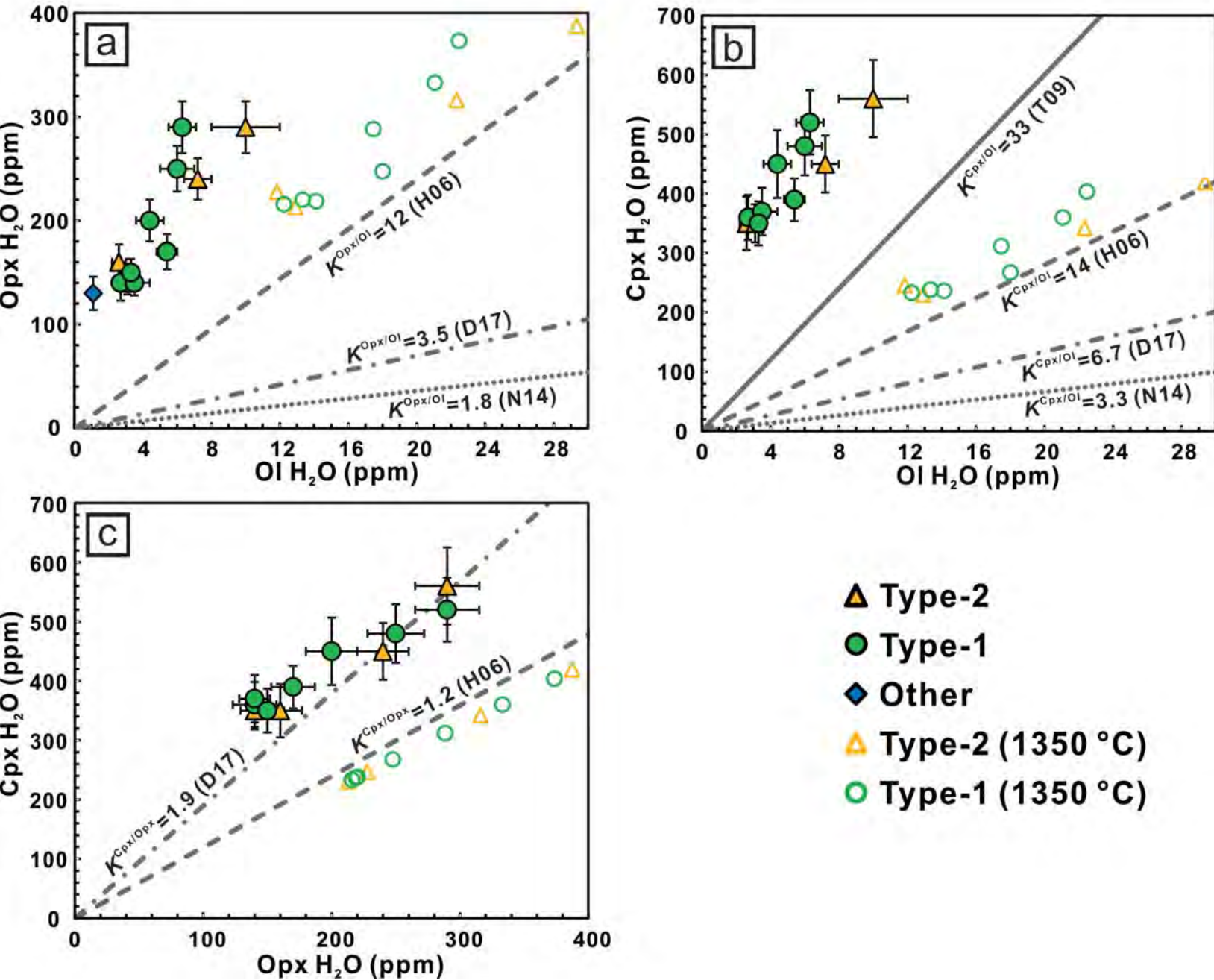
Figure 6
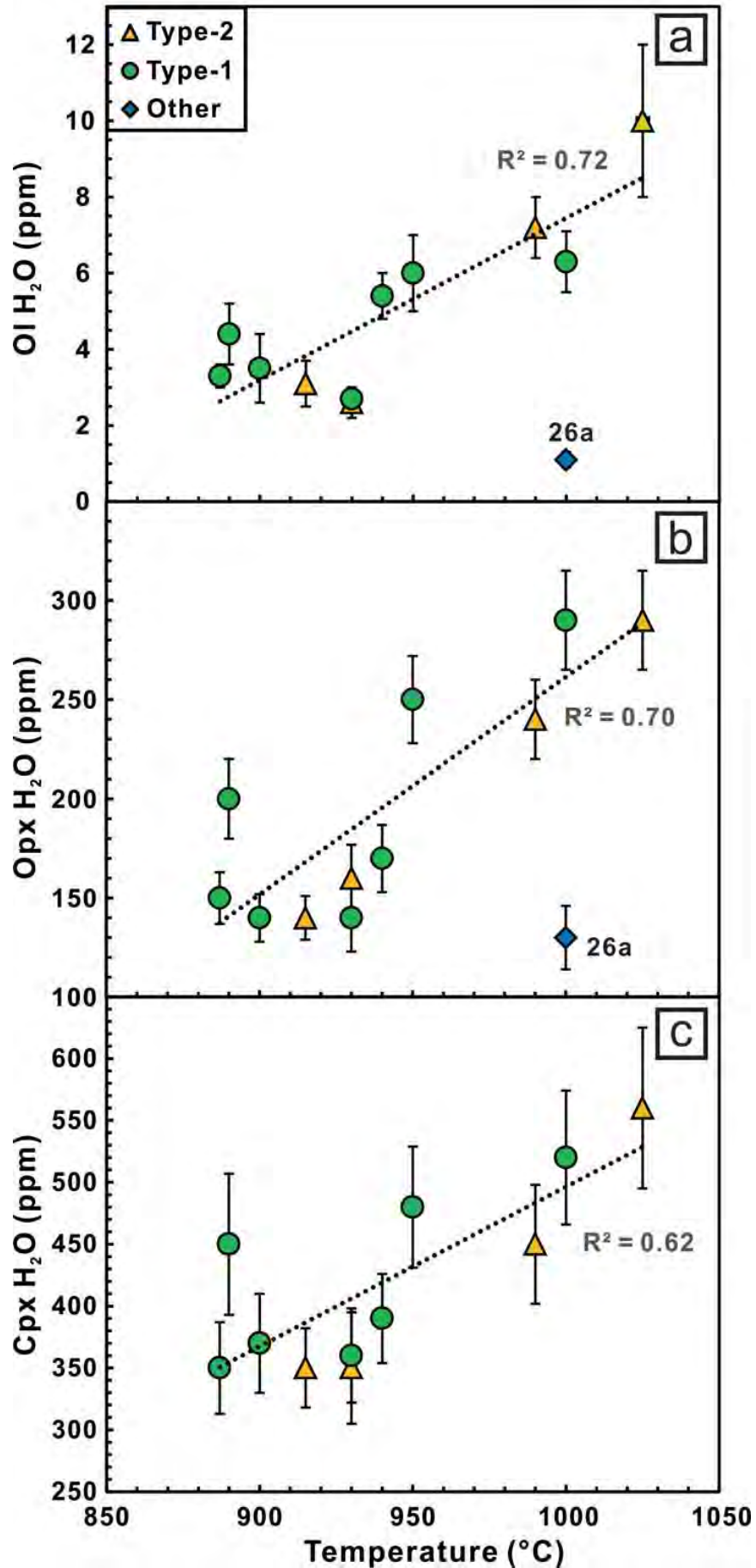
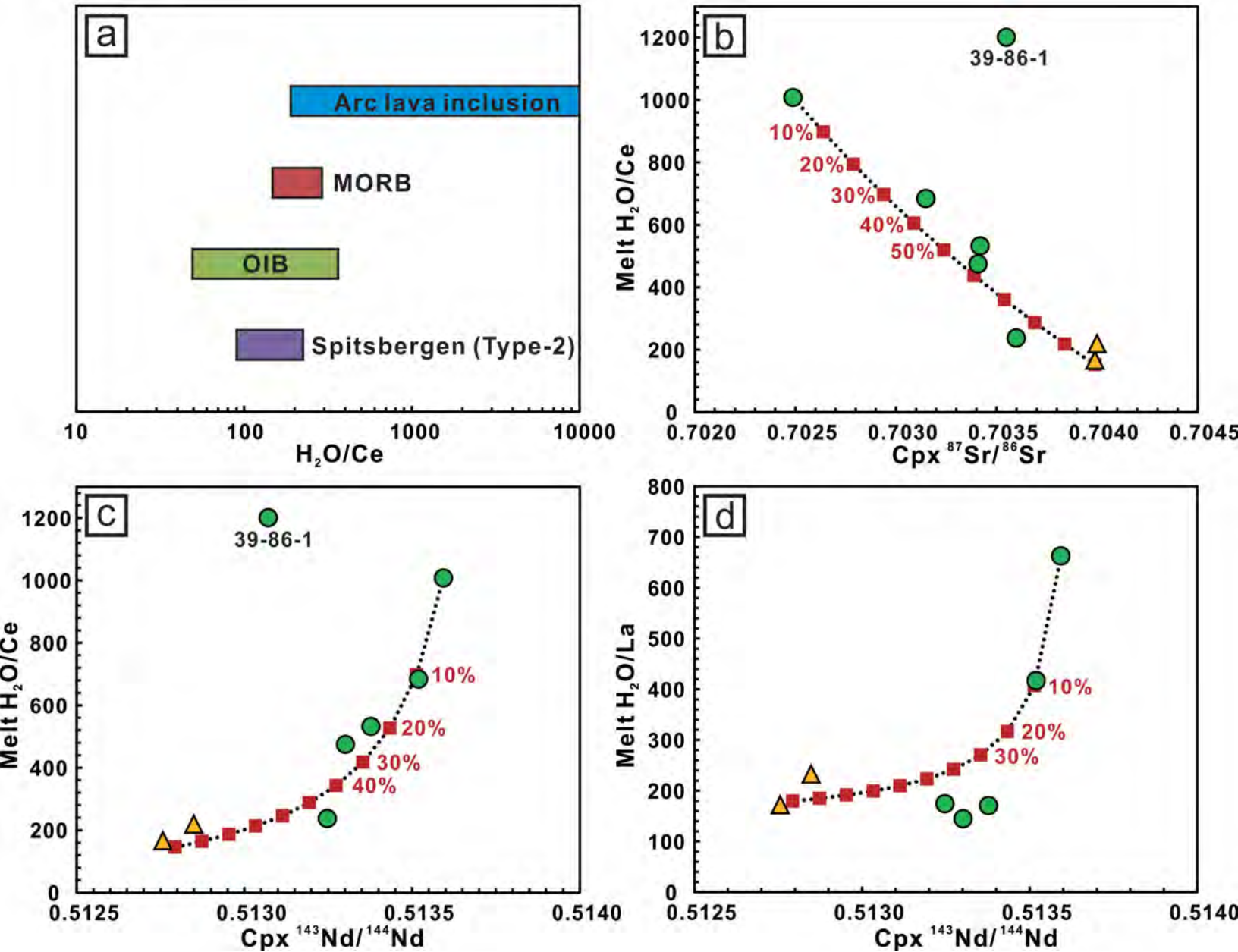Figure 7
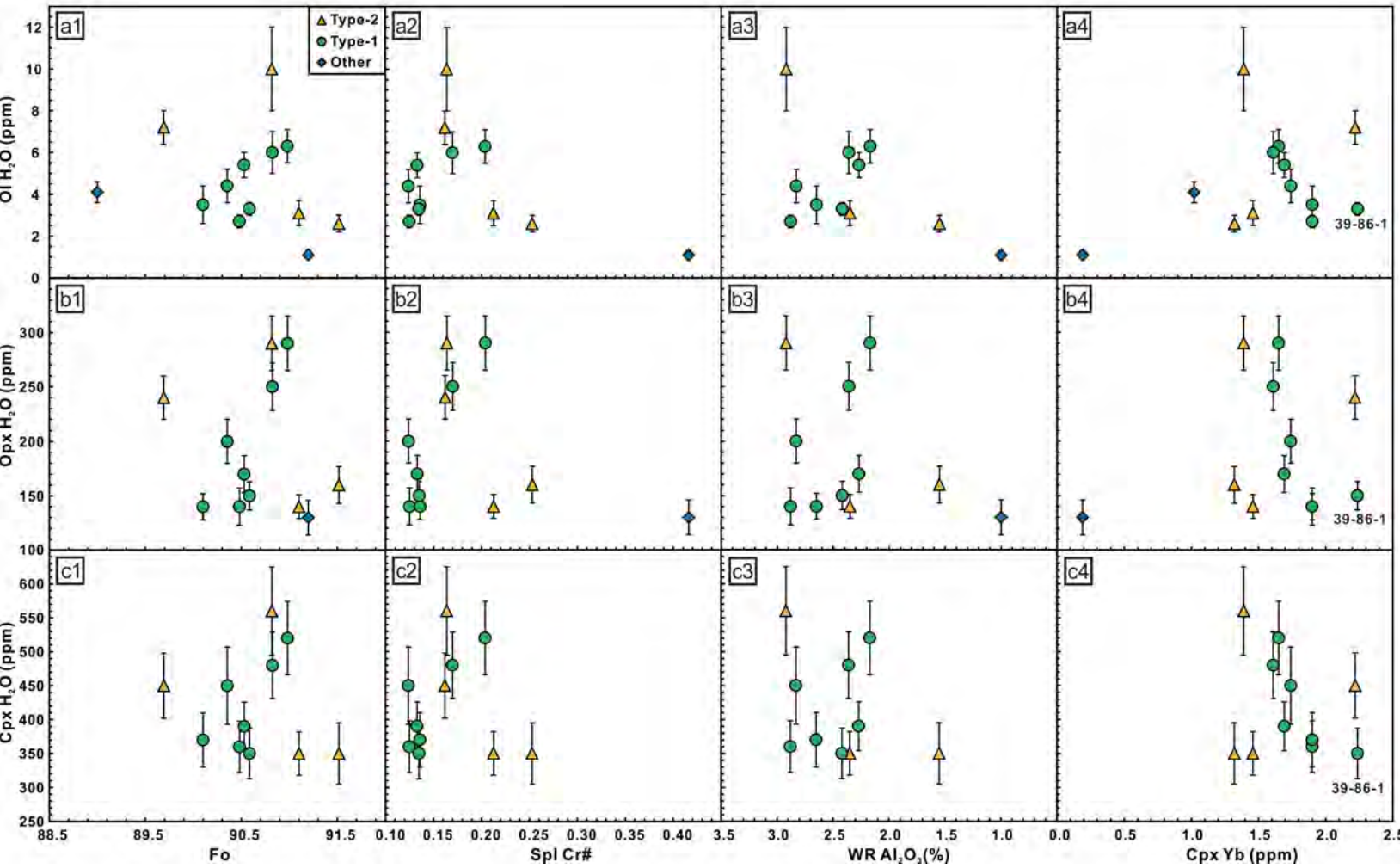
Figure 8
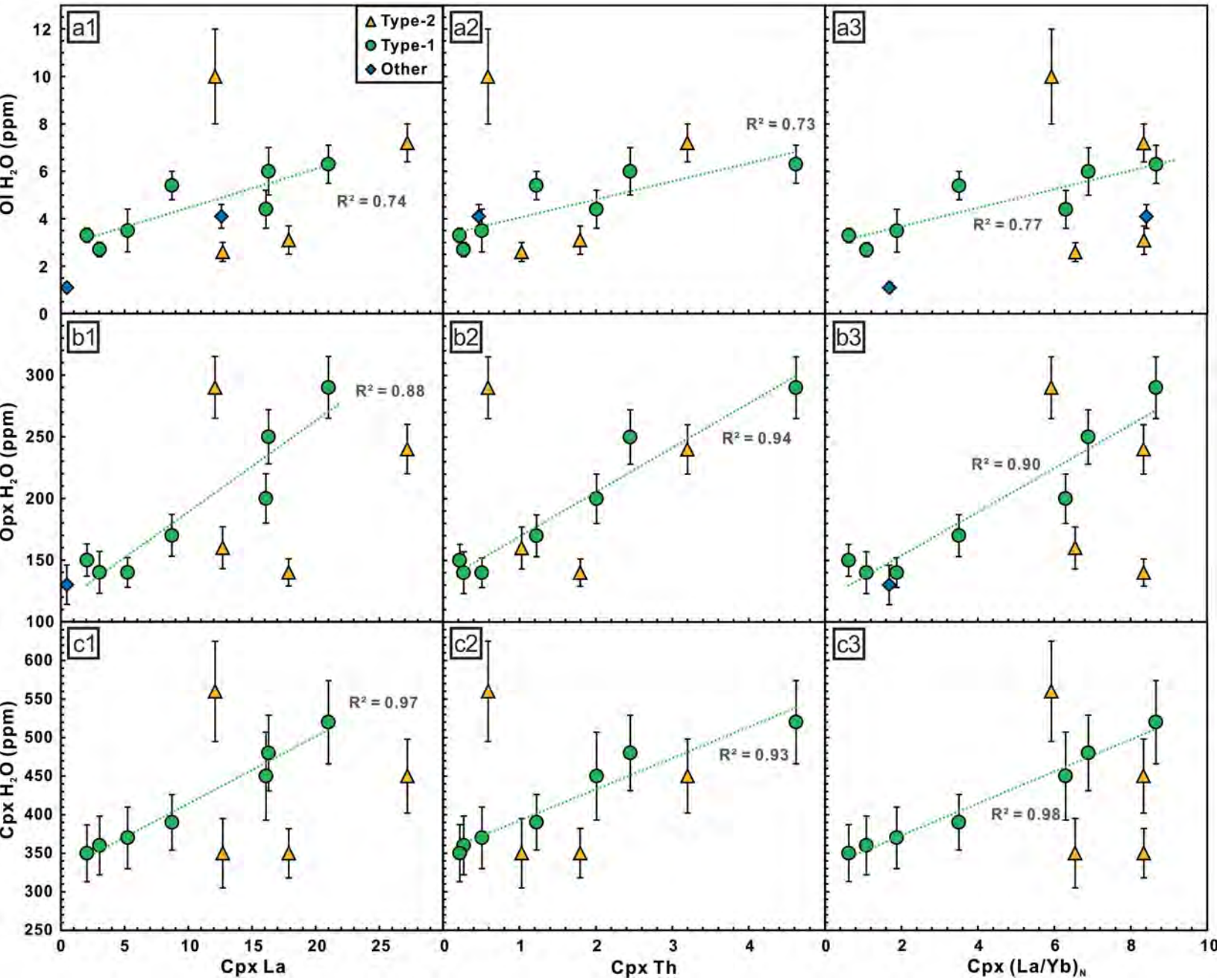
Figure 9
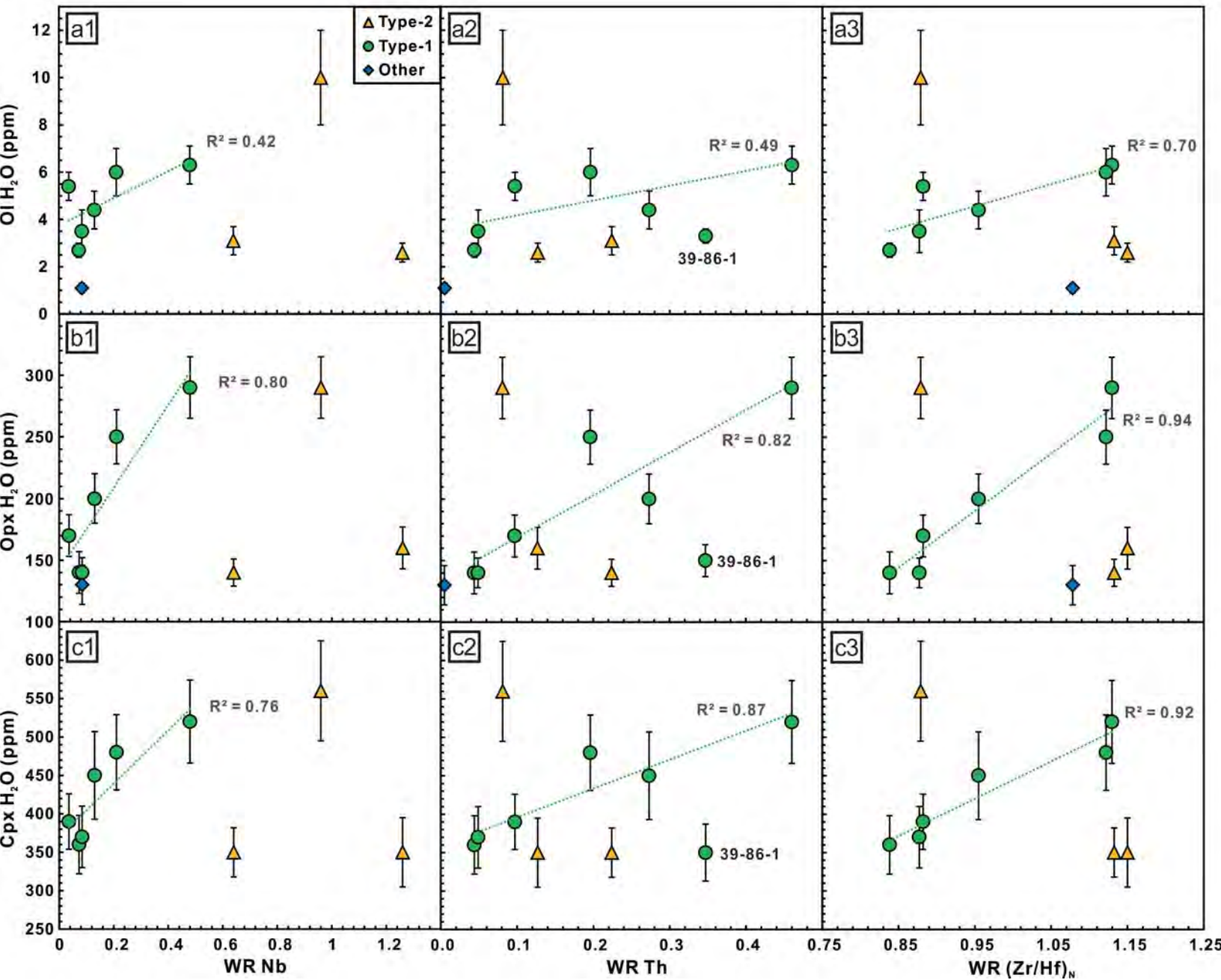
Figure 10
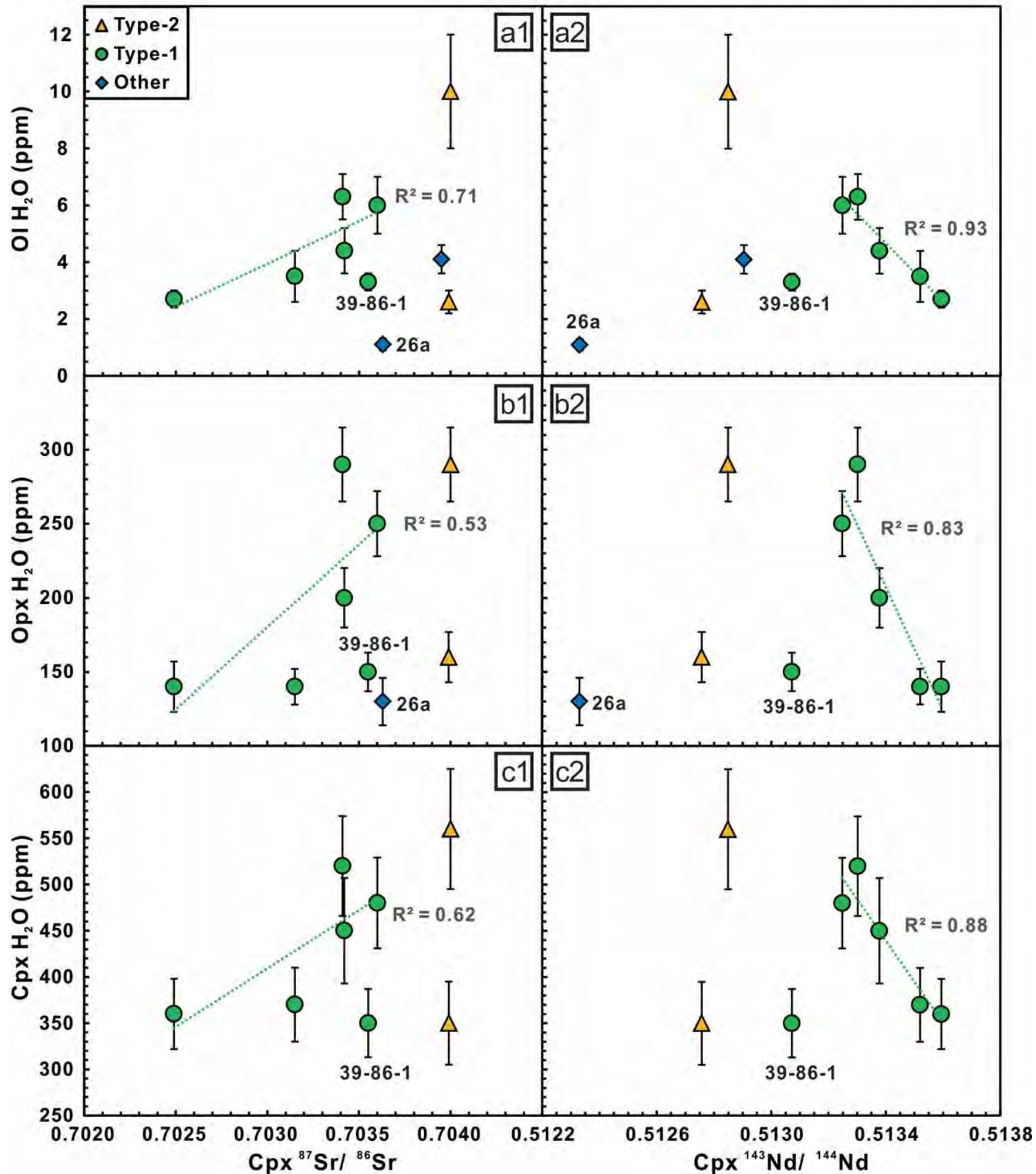
Figure 11

Figure 12

Figure 13